RICE UNIVERSITY

Terahertz Dynamics of Quantum-Confined Electrons in Carbon Nanomaterials

by

Lei Ren

A Thesis Submitted
in Partial Fulfillment of the
Requirements for the Degree

Doctor of Philosophy

Approved, Thesis Committee:

Junichiro Kono, Chair
Professor of Electrical and Computer Engineering and Professor of Physics and Astronomy

Daniel M. Mittleman
Professor of Electrical and Computer Engineering

Kevin F. Kelly
Associate Professor of Electrical and Computer Engineering

Deceased

Richard E. Smalley
University Professor, Gene and Norman Hackerman Professor of Chemistry, and Professor of Physics and Astronomy, Co-Chair

Houston, Texas
December, 2011

ABSTRACT

Terahertz Dynamics of Quantum-Confined Electrons in Carbon Nanomaterials

by

Lei Ren

The terahertz (THz) frequency range, 0.1 - 20 THz, exists between the microwave and infrared ranges and contains abundant information on the dynamics of charge and spin carriers in condensed matter systems. Since its advent two decades ago, THz spectroscopy has been extensively used to study a wide range of solid state materials, including typical semiconductors, conducting polymers, insulators, superconductors, and artificially grown structures such as quantum wells. In these systems, electronic and photonic events tend to occur on the time scale of tens to hundreds of femtoseconds, which results in many important excitations, resonances and dynamical phenomena in the THz frequency range. In this dissertation work, we have developed a typical THz time-domain spectroscopy (TDS) system to investigate the THz dynamics of quantum-confined electrons in two important types of carbon nanomaterial: single-walled carbon nanotubes (SWNTs) and graphene.

Polarization dependent THz transmission measurements were conducted on a highly-aligned SWNT film on a sapphire substrate, revealing extremely high anisotropy: virtually no attenuation was observed when the polarization of the THz beam was perpendicular to the nanotube axis, while the THz beam was strongly absorbed when its polarization was parallel to the tube axis. From the measured absorption anisotropy, we calculated the reduced linear dichrosim to be 3, corresponding to a nematic order

parameter of 1. These observations are a direct result of the one-dimensional nature of conduction electrons in the nanotubes and, at the same time, demonstrate that any misalignment of nanotubes in the film must have characteristic length scales much smaller than the wavelengths used in these experiments (1.5 mm $-$ 150 μm). Based on this work, an ideal THz linear polarizer built with parallel stacks of such aligned SWNT films was synthesized, exhibiting a degree of polarization of 99.9% throughout the frequency range 0.2 $-$ 2.2 THz and a high extinction ratio of 10^{-3} (or 30 dB). The THz complex conductivity of the thin SWNT film was extracted through a proper model directly from the TDS data without Kramers-Kronig analysis. Both real and imaginary parts of the conductivity showed a non-Drude frequency dependence, indicating the presence of plasmon-dipole resonance at higher frequencies.

Finally, the optical conductivity of large-area graphene grown from solid state carbon source was studied in a wide spectral range (7 cm^{-1} $-$ 9500 cm^{-1}) using THz-TDS and Fourier transform infrared spectroscopy. We observed that the Fermi level E_f of graphene could be tuned by both electrical gating and thermal annealing. The optical conductivity measured at different carrier concentrations exhibited Drude-like frequency dependence, and different $2E_f$ onsets in the spectrum were probed as well.

Acknowledgments

It has been seven years since I started the graduate school. After considering how many seven years you have in your lifetime, you will find that this is really a long journey. Now, it is very close to the end. At this emotional moment, I would like to sincerely thank all those people who provided me with help during this exceptional journey.

First, I would like to express my greatest gratitude towards my supervisor, Prof. Junichiro Kono. When I just entered this laboratory, I was naive and had no previous research experience in this field. He brought me to the ultrafast and terahertz (THz) spectroscopy area, and taught me everything from basic semiconductor physics to professional and precise experimental skills, from how to make presentations and write papers to how to think and behave like a true scientist. Throughout my whole Ph.D. research, he constantly and patiently gave great support, guidance and encouragement to me despite frequent failures and unfruitful experiments. Having Prof. Kono as my Ph.D. advisor would be definitely one of the luckiest things for me in my whole lifetime.

Next, I would like to thank Prof. Daniel Mittleman and his group members for all kinds of technical advice and support for my THz system construction. I want to particularly thank Prof. Mittleman for serving on my committee and his generosity for providing me with THz emitters and detectors. I also appreciate Prof. Masayoshi Tonochi and his postdoc Dr. Kei Takeya in Osaka University, for their nice hospitalities when I took the short term research visit to their laboratory there in Japan, and their great generosity for offering me THz devices and setup assistance.

I would like to give my heartfelt thanks to Prof. Alexey Belyanin and his postdoc

Dr. Aleksander Wójcik at Texas A&M University for helping me with theoretical calculations, modelings and simulations for my experimental results.

I would like to thank Prof. Kevin Kelly for agreeing to serve on my thesis committee at the last moment.

I would also like to express loads of my thanks to our collaborators in Chemistry, Chemical Engineering and Materials Science Departments at Rice for the invaluable high-quality carbon nanomaterials samples provided for my research: Cary Pint and Francesca Mirri in Dr. Robert Hauge's group for the highly aligned single-walled carbon nanotube (SWNT) films, Zhengzong Sun, Zheng Yan, Dr. Zhong Jin, Changsheng Xiang and Jun Yao in Prof. James Tour's group for the large-area graphene films, aligned graphene fibers and graphene FET device, Colin Young, Natnael Behabtu, and Budhadipta Dan in Prof. Matteo Pasquali's group for the aligned highly conductive carbon nanotube fibers and metallic enriched SWNTs films, and Dr. Li Song, Dr. Zheng Liu, Lulu Ma and Shizhen Zhao in Prof. Pulickel Ajayan's group for different types of graphene samples. Without these excellent samples, it would have been absolutely impossible for me to get meaningful THz spectroscopy results.

I am truly indebted to all group members in the Kono lab, for providing me with an ideal place to study and do research in and feel like a home. In particular, I thank the former group members Dr. Xiangfeng Wang and Dr. David Hilton, who led me to the optical table and taught me the THz techniques and experimental skills on optics from basic to advanced, step by step and question by question. They made me grow up gradually in the lab from a kid to an adult. I thank Qi Zhang for his hard work on the Fourier transform infrared spectroscopy system and making it run nicely; he provided experimental results in the infrared range as a significant supplement to mine in the THz range. I also thank Sasa Zaric, Erik Hároz, Jonah Shaver, Ajit Srivastava, Chanjuan Sun, Dr. Yoichi Murakami, Thomas Searles, William Rice, Darius Morris, Layla Booshehri, Tim Noe, Michelle Jin, Takashi Arikawa, Sebastien Nanot, Xuan Wang, Jihee Kim and Xiaowei He. The precious time we spent together and the

beautiful moments we shared through all these years in lab will be cherished in my memory forever together with their smiling faces. I would also like to thank Ms. Sarah Phillips for taking care of all different issues and making our group well organized and run smoothly.

I would like to thank all the known and unknown people at Rice who make the campus beautiful and my graduate study enjoyable.

Finally and most importantly, I thank my parents Mr. Shunqing Ren and Mrs. Shaoling Shi in China, for their everlasting love and support for me, and they have sacrificed so much for me all through my life. I also thank my girlfriend (also future wife) Ms. Wenjun Zhu for her persistent love and trust on me, and her sweet and insistent company during these two years as well; she has devoted a lot to my career, too. To them, my beloved family members, I dedicate this thesis.

Contents

Abstract ii

Acknowledgments iv

List of Illustrations x

List of Tables xix

1 Introduction 1

1.1 Carbon nanomaterials for optoelectronics 1

1.2 Carbon nanomaterials for basic studies of low-dimensional electrons . 3

1.3 Optical Conductivity 4

1.3.1 Definition 4

1.3.2 Quantitative Description 5

1.4 Scope of thesis 7

2 Terahertz Time-Domain Spectroscopy 8

2.1 THz/FIR Frequency Range 8

2.2 Principles of THz-TDS 8

2.2.1 THz Emitter 9

2.2.2 THz Detector 13

2.3 Characterization of the THz-TDS System 16

2.3.1 Gaussian beam profile tracing 16

2.3.2 Standard sample measurement – n-type silicon wafer 19

2.4 Advantages of THz-TDS 23

3 Physics of Low-Dimensional Carbon Nanomaterials 26

3.1 Crystal and Electronic Energy-Band Structure 26
3.1.1 Graphene 26
3.1.2 Single-Walled Carbon Nanotubes 31
3.2 Optical Properties 37
3.2.1 Single-Walled Carbon Nanotubes 37
3.2.2 Graphene 42
3.3 Terahertz Dynamics 45
3.3.1 Single-Walled Carbon Nanotubes 45
3.3.2 Graphene 48

4 Samples and Experimental Methods 55
4.1 Samples 55
4.1.1 Highly aligned SWNT films 55
4.1.2 Large-area solid-state-grown graphene 58
4.2 THz-TDS system components 60
4.2.1 Ti:Sapphire Laser 60
4.2.2 Optical delay line 62
4.2.3 THz emitter and detector 63
4.2.4 Preamplifier and lock-in amplifier 64
4.2.5 Purging box and sample holder 65

5 Experimental Results I : Carbon Nanotube THz Polarizer 69
5.1 Conventional industrialized wire-grid THz polarizer 69
5.2 Carbon nanotube THz polarizer 70
5.3 Experimental configuration 70
5.4 Results 72
5.4.1 Strong anisotropic THz responses 72

5.4.2 Extremely high alignment of the SWNTs 73
5.5 Further improvements – an ideal THz polarizer 77
5.5.1 SWNTs film stacks and their THz resposes 77
5.5.2 Ideal DOP and ER 81
5.5.3 Comparison with wire-grid THz polarizer 81

6 Experimental Results II : Dynamic Conductivity Tensor of Aligned Carbon Nanotube Films 86
6.1 One-dimensional dynamics and AC conductivity of SWNTs 86
6.2 Quantitative model and equation development 88
6.3 Frequency dependent anisotropic THz conductivity 90
6.4 Theoretical modeling and fitting 90
6.5 Broad FIR absorption peak 97

7 Experimental Results III : Fermi Level Probing and Controlling in Graphene 100
7.1 Fermi level tuning in graphene 100
7.2 Tunable E_f via electrical gating 102
7.2.1 Experimental configuration and modulated THz waves 102
7.2.2 Drude-like intraband conductivities 104
7.3 Fermi energy tuning via thermal annealing 108
7.4 Graphene sample quality effects 112

8 Conclusions and Future Work 116
8.1 Conclusions 116
8.2 Future Work 118

Bibliography 120

Illustrations

2.1 Schematic diagram of a THz-TDS system using a femtosecond pulsed laser 10

2.2 Typical structure of photoconductive antenna THz emitter. 11

2.3 The physical response of a voltage-biased photoconductive antenna to a focused femtosecond laser pulse: induced photocurrent by the focused optical pulse and radiated THz field according to Maxwell's equations. 12

2.4 Optical rectification for THz generation through a <110> ZnTe nonlinear crystal. 13

2.5 THz detection process from photoconductive antenna detector. 14

2.6 THz waveform mapping through changing the relative time-delay between the probing laser pulse and the to-be probed THz pulse. . . . 15

2.7 Typical THz (a) waveform in the time-domain and (b) amplitude spectrum in the frequency domain. 15

2.8 Schematic illustration of the razor-blade method for Gaussian beam profile tracing, basically blue color represents for the "blocked" and red for the "unblocked". 17

2.9 Gaussian beam profiling result via razor-blade method, with red circles for experimental data and blue line for theoretical fitting. . . . 18

2.10 Transmission analysis diagram for the thick medium silicon wafer. . . 20

2.11 Time-domain THz waveforms transmitted through the n-type silicon sample (red) and air reference (blue). 22

2.12 Frequency domain spectra of the n-type silicon sample (red) and air reference (blue): (a) amplitude spectrum, and (b) phase spectrum . . 22
2.13 THz dynamics of the n-type silicon sample: (a) real part of refractive index, (b) imaginary part of refractive index, (c) real part of conductivity, and (d) imaginary part of conductivity 24

3.1 (a) Graphene (b) Crystalline lattice structure of graphene, $\boldsymbol{a}_1$ and $\boldsymbol{a}_2$ are the lattice unit vectors, and δ_i, $i = 1, 2, 3$ are the nearest neighbor vectors. 27
3.2 Brillouin zone. The Dirac points are located at the $\boldsymbol{K}$ and $\boldsymbol{K}'$ points. Reproduced from Ref. [57]. 28
3.3 Electron energy band of graphene obtained under tight-binding approximation, with $t = 2.7$ eV and $t' = 0.2t$. Energy is in unit of t. Right: zoom-in of the energy bands around one of the Dirac points. Reproduced from Ref. [57]. 29
3.4 Cyclotron mass of charge carriers in graphene as a function of their concentration n. Positive and negative n correspond to electrons and holes, respectively. Reproduced from Ref. [36]. 30
3.5 Single-walled carbon nanotube is built by rolling up a single-layer 2D graphene sheet. Adapted from Ref. [35]. 32
3.6 (a)The geometry of how 2D graphene sheet is rolled up to SWNT, and the definitions of different chirality quantities. (b) The relation between chiralities (n, m)s and the SWNTs species. Reproduced from Ref. [60] 33

3.7 The hexagons in blue lines are 2D graphene Brillouin zones. The wave vector k for 1D SWNT as red lines for (a) metallic and (b) semiconducting SWNTs. In the direction of $\boldsymbol{K}_1$, discrete k values are obtained by periodic boundary conditions for the SWNT circumferential direction. (a) For metallic SWNT, red line intersects a K point at the Fermi level of graphene. (b) For semiconducting SWNT, the K point always stands one-third of the distance between two red lines. 35

3.8 1D density of states for metallic (left) and semiconducting (right) SWNT, together with their electronic energy bandstructures, and several most common optical transitions between van Hove singularity subbands: E_{11}^M, E_{11}^S, E_{22}^S, and E_{33}^S 36

3.9 Optical absorption spectra for four types of SWNTs with different diameter distributions. The inset shows their corresponding RBM modes of Raman spectroscopy obtained at 488 nm laser excitation, which estimate the diameter distribution. Adapted from [64]. 38

3.10 (a) Optical absorption spectrum of individualized CoMoCAT SWNTs dispersed in DI water using TDC (red line) and SDBS (blue line) as surfactant. The absorption peaks from different SWNT species are assigned with their chirality indices (n, m). Adapted from [66] (b) Optical absorption spectra of metallic enriched HiPco SWNTs separated out through DGU (blue line) and their starting as-produced mixed HiPco SWNTs (red line). Reproduced from [67] . 40

3.11 (a) 1D density of states diagram of a semiconducting SWNT showing the photoluminescence process. (b) PLE map of a HiPco-grown SWNTs sample suspended in SDS and deuterium oxide. Reproduced from [69] 41

3.12 Electronic energy bandstructure of a typical p-doped graphene, illustrating the two types of optical behavior: intraband absorption (green arrows) and interband absorption (yellow arrows). 43

3.13 (A) Photograph of a 50-μm aperture with the suspended graphene partially covered, different optical opacities at different regimes are illustrated. (B) Optical transmittance of the single-layer graphene in visible range, inset shows the transmittance of the while light as a function of number of graphene layers. Reproduced from ref. [44] . . 45

3.14 Optical conductivity (proportional to optical absorption) spectrum in infrared range for mechanically cleaved graphene sample under different gate voltages. Reproduced from ref. [76] 46

3.15 (a) Real part of dynamic conductivity of laser-vaporization-grown SWNTs sample extracted from the IR reflectance spectrum, exhibiting a broad $\sim$ 4 THz absorption peak robust to temperature change. Adapted from Ref. [78]. (b) Polarized absorption spectra of pristine (black lines) and tetrafluorotetracyanoquinodimethane (F_4TCNQ)-doped (dashed lines) L-SWNTs films. The $\sim$ 4 THz absorption peak is dramatically enhanced in doped L-SWNTs without notable change in the peak position, while the optical absorption peaks are greatly suppressed there. Adapted from Ref. [83] 47

3.16 Real part of the optical sheet conductivity (gray), normalized by the universal optical conductivity value $\sigma_Q = \pi e^2/2h$: (a) buffer layer, (b) monolayer graphene, (c) multilayer graphene; (d) $-$ (f) 2.5 $\times$ 2.5 μm^2 LEEM images of nominally buffer, monolayer, and multilayer graphene. Reproduced from Ref. [89] 49

3.17 (a) and (b) Gate-voltage-induced AC conductivity change $\Delta\sigma'$ together with its Drude-model fitting in hole- and electron- doped graphene, respectively, in the range $30 - 450$ cm^{-1} ($0.9 - 13.5$ THz). (c) and (d) The scattering rate Γ and Drude weight D fit for different hole and electron concentrations. Reproduced from Ref. [46] 51

3.18 Gate-induced change of transmission spectra (red solid line) of aligned graphene micro-ribbon arrays, with the ribbon alignment parallel (a) and perpendicular (b) to the incident light polarization, together with the free carrier fitting by Drude model and plasmon resonance fitting by a Lorentzian lineshape. Inset shows an AFM image of a graphene micro-ribbon array sample with ribbon width of 4 μm and a ribbon-gap width ratio of 1:1. Adapted from Ref. [17] . . 52

3.19 Sketch of graphene bandstructure and energy distributions of photogenerated electrons and holes under interband optical pumping of photon energy $\hbar\Omega$. A cascade of phonons emission ($\hbar\omega_0$) is expected, so is the photon radiation ($\hbar\omega$) for sufficiently strong optical pumping. Reproduced from Ref. [38] 54

4.1 Highly aligned SWNTs film: (a) Growth of upright SWNT lines using patterned catalyst substrates, (b) contact transfer of aligned SWNTs films to THz transparent sapphire substrates, (c) image showing as-transferred aligned SWNTs films and growth substrate from which transfer occurred, (d) $-$ (e) scanning electron microscope and optical microscope images showing the excellent SWNTs alignment inside the transferred SWNT structures. 57

4.2 Growth of large-area graphene from solid-state carbon source and its transfer for spectroscopy study. 59

4.3 (a) Raman spectrum and (b) UV-Visible-NIR transmittance spectrum together with optical microscopy image for single-layer (red), bi-layer (pink), few-layer (green) and many-layer (blue) graphene samples. . . 61
4.4 Photograph of the Ti:Sapphire laser system. Left: Verdi solid-state green laser; Right: MIRA Ti:Sapphire laser. 62
4.5 Photograph of the optical delay line. Top: motion controller; Bottom: retro-reflector and time-delay stage. 63
4.6 Optical microscopy image of the dipole of one typical photoconductive antenna for THz emission or detection. 64
4.7 Current preamplifier (top) and lock-in amplifier (bottom). 65
4.8 Purging box for the THz-TDS system to avoid water absorption from air, with a homemade sample holder mounted on a 1D motorized stage inside it. 67
4.9 Photograph of entire THz-TDS system. 68

5.1 (a) Scanning electron microscope image of the highly horizontally aligned SWNTs film used in this experiment. (b) Sketch of the experimental configuration used, showing the interaction between the linearly polarized THz electric field and highly aligned SWNTs film. The angle between the THz polarization direction and the nanotube alignment direction, θ, was varied between 0° and 90° [96]. 71
5.2 (a) THz electric field signals in the time domain, (b) transmitted THz amplitude spectra obtained through Fourier transform of the time domain signals in (a), and (c) THz absorbance spectra for the reference sapphire substrate (black dashed curves) and for the SWNTs film for different polarization angles (colored solid curves) [96]. 74

5.3 (a) Parallel ($A_{//}$), perpendicular ($A_{\perp}$), and isotropic (A_0) absorbance, (b) LD and LD^r, and (c) degree of polarization calculated from absorbance values as a function of THz frequency [96]. 76

5.4 Scheme showing the use of multiple SWNTs films to produce high performance polarizers discussed in this work. 78

5.5 Anisotropic THz Transmission through SWNTs Polarizers: Transmitted THz electric field signals in the time domain for (a) single-layer SWNTs film with gaps, (b) single-layer SWNTs film without gaps, (c) double-layer SWNTs film and (d) triple-layer SWNTs film. Black dashed lines with open circles are for the reference sapphire substrates, blue solid lines are for samples with THz polarization parallel to the nanotube axis, and red solid lines are for samples with THz polarization perpendicular to the nanotube axis. On the right column, THz transmittance spectra in the $0.2 - 2.2$ THz range are shown for (e) single-layer SWNTs film with gaps, (f) single-layer SWNTs film without gaps, (g) double-layer SWNTs film, and (h) triple-layer SWNTs film. Blue solid lines with open circle markers are for the parallel case, and red solid lines with open square markers are for the perpendicular case. 80

5.6 Polarizer parameters for the SWNTs polarizers: (a) Degree of polarization and (b) extinction ratio of the THz polarizers with different thicknesses as a function of frequency in the $0.2 - 2.2$ THz range. For the optimized triple-layer SWNTs polarizer, the averaged value of the extinction ratio in this frequency range is 33.4 dB. 82

5.7 Prospects for future industrialization and commercialization: (a) Comparison between SWNTs polarizer and wire-grid polarizer on extinct ratio. (b) Comparison between SWNTs polarizer and wire-grid polarizer on degree of polarization. 84

6.1 Transmission analysis diagram for the thin-film-on-thick-substrate model. 89
6.2 (a) Real and (b) imaginary parts of the parallel and perpendicular elements of the dynamic conductivity tensor for the aligned SWNTs film extracted from the THz time-domain signals. 91
6.3 Theoretical fitting of the THz conductivity of the highly aligned SWNTs film using effective medium theory. Circles: experimental data, solid lines: theory. 94
6.4 Length distributions of two CNT species included in Eq. (6.8). Their total number densities $\bar{n}$ (in cm^{-3}) are indicated. 95
6.5 Contribution of long and short CNTs to the conductivity spectrum calculated with Eqs. 6.8. 96
6.6 THz & IR absorbance spectra of highly aligned SWNTs film, for both the parallel (blue) and perpendicular (red) cases. 98

7.1 Experimental configuration sketch of gate-voltage-dependent THz-TDS/FTIR transmission measurements on graphene/SiO_2/p-Si sample. 103
7.2 Gate-voltage-dependent THz-TDS/FTIR transmission measurements on graphene/SiO_2/p-Si sample: (a) transmitted THz waveforms through the graphene device under different applied gate voltages, (b) monotonic change of THz signals as the tunable gate voltage, (c) transmitted THz power (blue circled line) and DC resistance of graphene (red solid line) as a function of gate voltage. 105
7.3 Transmission analysis diagram for the 2D conducting sheet on a thick substrate 106

7.4 Dynamic conductivity of the large-area graphene in THz/IR frequency range under various gate voltages. (a) Real and (b) Imaginary part of the 2D sheet complex conductance for intraband conductivity. (c) $2E_f$ onsets in the MIR transmission spectrum for interband conductivity. 109

7.5 Graphene Fermi level shifted as the removal of chemical dopants: (a) THz/IR conductivity of the large-area graphene before (blue) and after (red) thermal annealing. (b) FET gating curve as a function of environment. 111

7.6 (a) Microscopy image showing a graphene sample full of dirty scattering centers. (b) Microscopy image indicating the ununiformity of layer number in one graphene sample. (c) Raman spectra of different spots on the sample shown in (b). (d) A zoomed-in of the G′ peaks in (c) 113

7.7 Comparison of the THz & IR dynamic conductivities between a "clean" graphene sample and a "dirty" graphene sample 114

Tables

6.1 Parameters used in the fitting distributions. 97

Chapter 1

Introduction

This dissertation work investigates carrier dynamics in two important types of low-dimensional carbon nanomaterials: single-walled carbon nanotubes (SWNTs) and graphene using terahertz (THz) time-domain spectroscopy (TDS) as the experimental tool.

1.1 Carbon nanomaterials for optoelectronics

The discoveries of C_{60} fullerene by Kroto and co-workers in 1985 [1] and carbon nanotubes (CNTs) by Iijima in 1991 [2] following a preliminary carbon filamentous growth work [3] have opened a new scientific revolution for nanotechnology, which promises that human beings can manipulate molecules and devices in nanometer (10^{-9} m) scales. Since then, an enormous amount of research has been done on its representative carbon nanomaterials, mostly single-walled carbon nanotubes (SWNTs), discovered in 1993 [4, 5], and graphene, first isolated in 2004 [6].

Although silicon and some other conventional III-V semiconductors have dominated solid-state optoelectronics for several decades, CNTs and graphene are right on their way to replace them because of their superb optoelectronic properties.

Photon detectors work based on the principle that the photons are absorbed by a semiconducting material and then the photogenerated electrons and holes produce a current or voltage across the device. A field-effect transistor (FET) based on a

single SWNT was demonstrated to work well as such a photoconductive detector [7]. In another way, a temperature change due to illumination with visible or IR light could also cause an electrical response due to a resistance change, and a film of CNTs was also reported to hehave as such a bolometer [8]. Fighting for the human energy challenges, CNTs have been also synthesized into photovoltaic devices or solar cells in order to realize power conversions, such as CNT composites in a photoactive layer [9], CNTs as a transparent electrode [10], and CNTs in dye-sensitized solar cells [11].

Owing to its unique optical and electronic properties, together with the mechanical robustness, functional flexibility and chemical/environmental stability, graphene has been even more intensively developed for applications in optoelectronics [12]. First, its high electrical conduction and optical transparency have made it a great candidate for electrodes of solar cells [13–15]. The Avouris group at IBM has demonstrated ultrafast transistor-based photodetectors made from single- and few-layer graphene. There, the generation and transport of photocarriers differ fundamentally from those in photodetectors made from conventional semiconductors due to the unique photonic and electronic properties of graphene, which results in a remarkably high bandwidth, zero source-drain bias and dark current operation, and good internal quantum efficiency [16]. The Wang group at the University of California at Berkeley has explored plasmon excitations of the two-dimensional (2D) massless Dirac electrons in graphene by synthesizing a device made of aligned graphene micro-ribbon arrays and tuning its ribbon width and in-situ electrostatic doping, and observed a frequency-tunable prominent plasmon resonance at room temperature in the THz/FIR frequency range [17].

1.2 Carbon nanomaterials for basic studies of low-dimensional electrons

Not only attracting much attention for future applications in micro-nano scale opto-electronic devices, from a fundamental point of view, these carbon nanomaterials are considered to be one of the most ideal systems that exhibit the quantum mechanical nature of interacting low-dimensional electrons.

SWNTs have been attracting considerable research interest for their unusual physical, chemical, electrical and mechanical properties since their discovery in 1993 [4, 5, 18–20]. SWNTs represent one of the most direct realizations of a 1D electron system available today and provide an ideal model 1-D condensed matter system in which to address fundamental theoretical questions in many-body physics. This 1D character of confined carriers and phonons in SWNTs leads to extremely anisotropic electric, magnetic, and optical properties [20]. Individual metallic SWNTs have been shown to be excellent quantum wires with very long coherence lengths [21], while individual semiconducting SWNTs have been shown to strongly absorb and emit light only when the light polarization is parallel to the tube axis [22]. Moreover, individualized SWNTs, both metallic and semiconducting, have been shown to align well in an external magnetic field [23–28] due to their anisotropic magnetic susceptibilities [29–31], and aligned SWNTs exhibit strong linear dichroism due to their anisotropic optical properties. Even in bundled samples where SWNTs form aggregates through van der Waals attraction, their anisotropic properties are expected to be preserved to a large degree, even though systematic optical spectroscopy studies have been limited [32–34] due to the rarity of ensemble samples in which the SWNTs are highly aligned. In Chapter 4, we describe our highly-aligned SWNTs film samples that are perfectly

suited for 1D character research, and discuss our THz-TDS experimental results on them in Chapter 5 and Chapter 6.

Graphene has been one of the most intensively studied research objects since its first isolation in 2004, especially due to its spectacular electronic properties [6, 35, 36]. This zero-gap semiconductor, consisting of a single layer of sp^2-bonded carbon atoms arranged into a 2D honeycomb lattice, possesses a photon-like, linear energy dispersion spectrum, which leads to electrons and holes of zero effective mass that behave like relativistic particles. They are called "Dirac fermions" (DFs) and expected to lead to exceptionally nonlinear electro-dynamic properties [37, 38]. A wide range of excellent experimental studies have been performed to investigate those unique 2D DFs in graphene, including direct probing of the massless DFs [39, 40], an anomalous quantum Hall effect [36, 41], Klein tunnelling [42, 43] in electrical transport, a universal optical conductivity and tunable interband transitions [44, 45] in optical response, and the intraband conductivity in the THz/FIR range [46], and remarkable plasmonic excitations [17].

1.3 Optical Conductivity

1.3.1 Definition

Optical conductivity, also known as dynamic conductivity or AC conductivity, as opposed to static conductivity or DC conductivity, is defined as the conductivity of a medium as a function of frequency. While the DC conductivity characterizes the overall electron transport behavior, the frequency dependence of the AC conductivity contains important information on scattering events and interactions. These effects can influence the frequency and temperature dependence of the conductivity some-

times in a very specific way. For example, theoretical studies based on Luttinger liquid have suggested that the optical conductivity of metallic carbon nanotubes should exhibit the so-called $\frac{\omega}{T}$ scaling [47, 48]. However, experimental studies in this direction have been very limited so far.

1.3.2 Quantitative Description

In this sub-section, a quantitative description of optical conductivity is introduced [49].

When a homogenous medium is illuminated by an external electric field, a charge redistribution occurs and then a current is produced. Such induced currents are proportional to the inducing small-enough fields, as the following equation expressed in the frequency spectrum

$$\boldsymbol{J}(\omega) = \sigma(\omega)\boldsymbol{E}(\omega), \tag{1.1}$$

where $\boldsymbol{J}$ and $\boldsymbol{E}$ are the total current and electric field, ω stands for the interacting optical frequency, and σ, of course, is the optical conductivity we are investigating.

Under the conditions used in the derivation of Eq. (1.1), the dielectric function $\epsilon(\omega)$ is defined as relating the (coarse-grained) electrical displacement $\boldsymbol{D}$ to the (coarse-grained) electric field $\boldsymbol{E}$,

$$\boldsymbol{D}(\omega) = \epsilon(\omega)\boldsymbol{E}(\omega). \tag{1.2}$$

The dielectric function can be directly expressed in terms of the optical conductivity,

$$\epsilon(\omega) = 1 + \frac{4\pi i\sigma(\omega)}{\omega}. \tag{1.3}$$

Note that here $\sigma(\omega)$ has the dimension of frequency, which means is in the Gaussian unit system. For a later convenient experimental use, we turn it into the SI unit

system by $\epsilon \rightarrow \epsilon/\epsilon_0$ and $\sigma \rightarrow \sigma/(4\pi\epsilon_0)$

$$\epsilon_{\mathrm{SI}}(\omega) = \epsilon_0 + \frac{i\sigma(\omega)}{\omega}, \tag{1.4}$$

where $\epsilon_0 = 8.85 \times 10^{-12}$ Fm^{-1} is the permittivity of free space.

The refractive index $n(\omega)$ of the medium studied can be obtained through a proper model after optical transmission experiments. In general, it should be complex and related to the dielectric function $\epsilon(\omega)$ by

$$n(\omega) = \sqrt{\epsilon(\omega)} = N(\omega) + i\kappa(\omega), \tag{1.5}$$

where $N(\omega)$ and $\kappa(\omega)$ are the real and imaginary parts of $n(\omega)$, and they characterize the dispersion (phase shift) and absorption (amplitude dissipation) of the light-medium interaction, respectively.

Then, through Eq. (1.4) one obtains the optical conductivity $\sigma(\omega)$, which should be also generally complex and can be expressed as

$$\sigma(\omega) = \sigma'(\omega) + \sigma''(\omega), \tag{1.6}$$

where $\sigma'(\omega)$ and $\sigma''(\omega)$ are the real and imaginary parts of the optical conductivity, respectively.

From Eqs. (1.4) and (1.5), we can see that $\sigma'(\omega)$ is largely determined by light absorption while $\sigma''(\omega)$ is determined by light dispersion. For incoherent measurements, one only gets the transmission (or absorption) of the sample and then could only obtain the real part of optical conductivity and lose its imaginary part, which should be extracted from the real part through the Kramers-Kronig (KK) relation. However, THz-TDS measurements provide us with both the amplitude and phase information of the THz electromagnetic wave, and allow us to get both real and imaginary parts of the optical conductivity without laborsome and somehow uncertain KK tranformations.

1.4 Scope of thesis

In Chapter 2, we describe the basic concepts of the THz-TDS technique, how it works for this project, and its advantages. The strongly anisotropic THz response of SWNTs is the result of their one-dimensional (1D) nature, and the exceptional THz and infrared (IR) dynamic conductivity behavior of graphene arises from its photon-like, linear energy dispersion spectrum. Thus, a theoretical background of SWNT and graphene properties such as their crystal-structure-dependent electronic bandstructures, light interaction and optical properties with a focus on the THz/IR range is presented in Chapter 3, together with some previous THz/IR work that has been done on these subjects. In Chapter 4, we describe the details of the SWNTs and graphene samples studied as well as the experimental setup used.

The main experimental results and accomplishments are discussed in the following three chapters. In Chapter 5, extremely anisotropic THz absorption of the highly aligned SWNTs films are demonstrated, together with a prospect for their future industrialization as linear THz polarizers. The dynamic conductivity tensor of the SWNTs thin film is extracted through a proper model and showed in Chapter 6. Theoretical analysis is presented, which suggests that there exist 1D plasmas along the nanotube axis. In Chapter 7, our most recent work on the graphene is presented, where the Fermi level is controlled by both electrical and chemical doping.

Finally, in Chapter 8, I summarize my research work and propose some future work on the projects.

Chapter 2

Terahertz Time-Domain Spectroscopy

2.1 THz/FIR Frequency Range

The terahertz (THz) frequency range covers the spectral range from about ~ 3 cm^{-1} to ~ 600 cm^{-1}, which is also known as the far-infrared (FIR) region of the spectrum. This implies frequencies on the order of about 0.1 to 20 THz, or photon energies from 0.41 meV to 82 meV, since 1 THz $\Longleftrightarrow$ 33.33 cm^{-1} $\Longleftrightarrow$ 300 μm $\Longleftrightarrow$ 4.1 meV in the language of optics. This frequency bridges the gap between microwave and infrared techniques, both of which have already been well developed and widely studied for a long time, while the techniques for this THz gap has been in a slumber status until a radical change happened in 1988/1989 after people's long fight for the generation and detection of ultrashort electrical transients: radiated electromagnetic (EM) pluses on scale of sub-picosecond were reported to propagate through free space from an emitter to a detector [50–52]! Since its born then, THz spectroscopy has attracted tremendous research for both its own techniques and its applications on probing the abundant information for condensed matter physics in this particular range.

2.2 Principles of THz-TDS

Figure 2.1 shows a schematic diagram of a typical THz time-domain spectroscopy (TDS) system. It consists of a femtosecond pulsed laser, a beam splitter, a time-delay line, a THz emitter, four parabolic mirrors (or two polyethylene lenses instead),

the solid state film sample to be measured, a THz detector, a current amplifier, a lock-in amplifier, a computer and some necessary mirrors as well. The pulsed laser beam from the Ti:Sapphire femtosecond laser is split into two by the beam splitter. One passes through a mechanically running chopper and goes to the THz emitter to generate THz radiation, while the other passes through the time-delay line and goes to the THz detector to probe the transmitted THz wave. The generated THz wave is collimated by the first off-axis parabolic mirror and focused by the second parabolic mirror on the sample. The THz wave interacts with the sample and then is collected by the third parabolic mirror. The collimated THz beam is finally focused by the fourth parabolic mirror onto the THz detector. The THz wave is then detected and converted into a current signal. The current signal is amplified and sent to the lock-in amplifier, and recorded by the computer.

2.2.1 THz Emitter

The THz emitter is the core of the entire THz-TDS system, and people have been devoting loads of efforts to develop newer and better THz generation techniques in order to get THz time-domain waves of higher intensity and especially broader bandwidth.

So far, the THz emission technique has experienced three major generations: (I) photoconductive antennas [50], (II) nonlinear electro-optic crystal [53], and (III) air plasma [54]. Here in this thesis, we will talk about the first two, which were used in our THz-TDS study on low-dimensional carbon nanomaterials.

Figure 2.2 shows the typical structure of a photoconductive antenna THz emitter, consisting of two metal lines (here in for ours it is gold) deposited on a low-temperature-grown GaAs substrate, which provides photocarriers with shorter life-

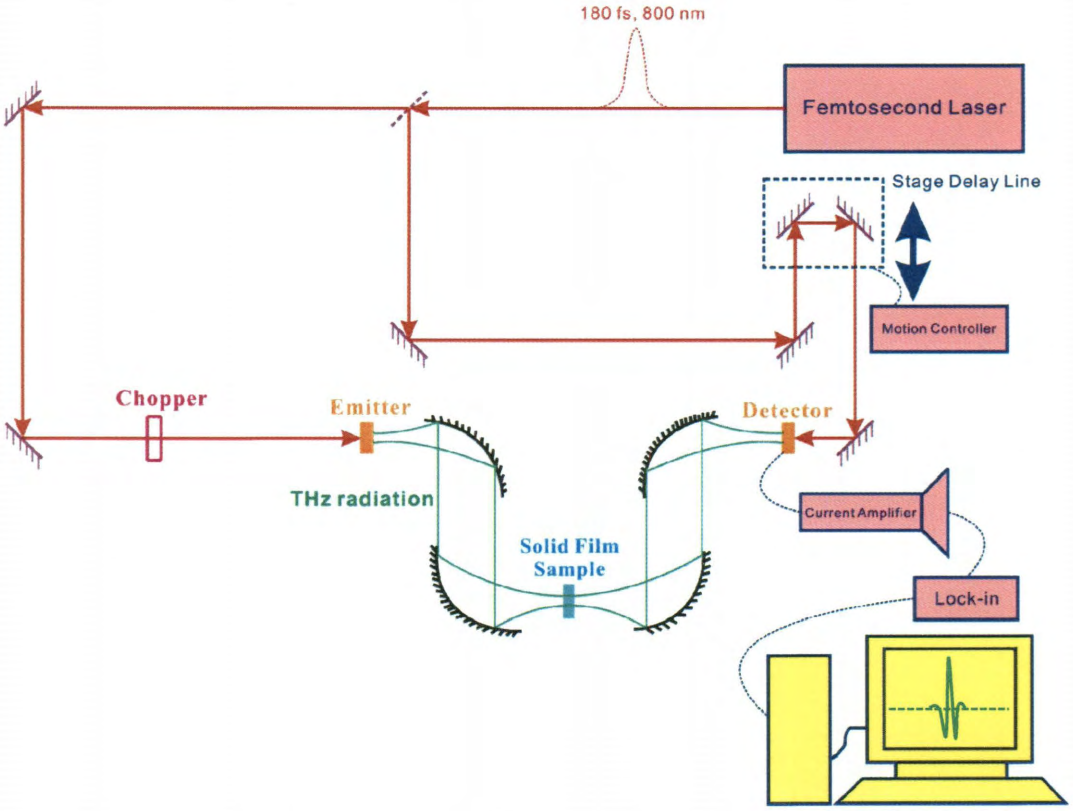

Figure 2.1 : Schematic diagram of a THz-TDS system using a femtosecond pulsed laser

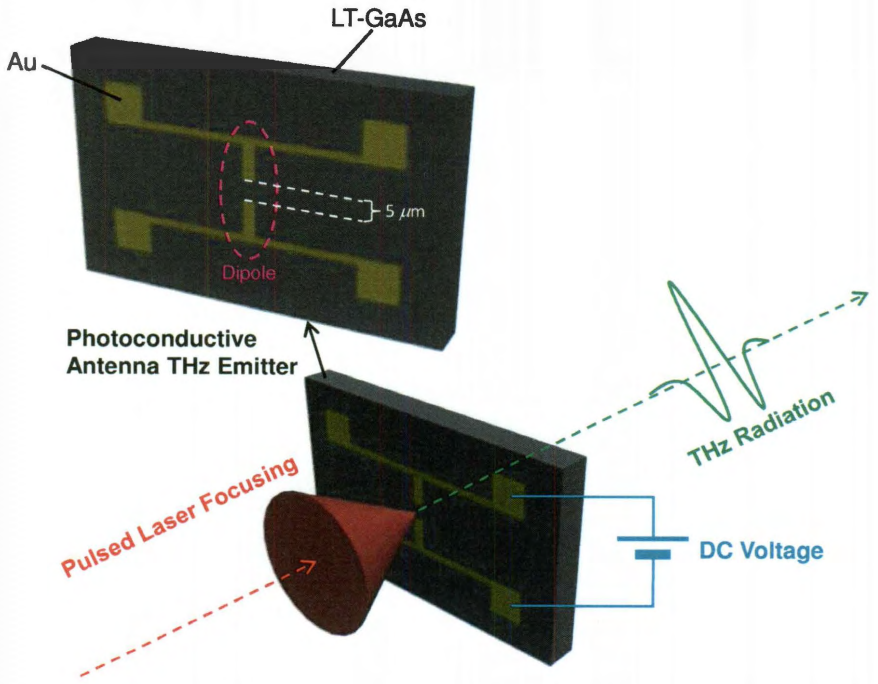

Figure 2.2 : Typical structure of photoconductive antenna THz emitter.

times. There is a dipole in the middle of the two metal lines with a tiny separation of 5 μm.

The femtosecond pulsed laser beam is focused onto this dipole gap to generate a THz radiation as schematically shown in Fig. 2.2. A DC voltage of about 15 V is applied across the two metal lines (then the across the dipole), creating a very strong electric field of $\sim$3 V/μm. Photocarriers are generated around the dipole gap by the high-intensity focused femtosecond laser pulses, and then accelerated at an enormous rate driven by the electric field to form a photocurrent. The photocurrent rises very rapidly after the injection of photocarriers and then decays with the carrier lifetime.

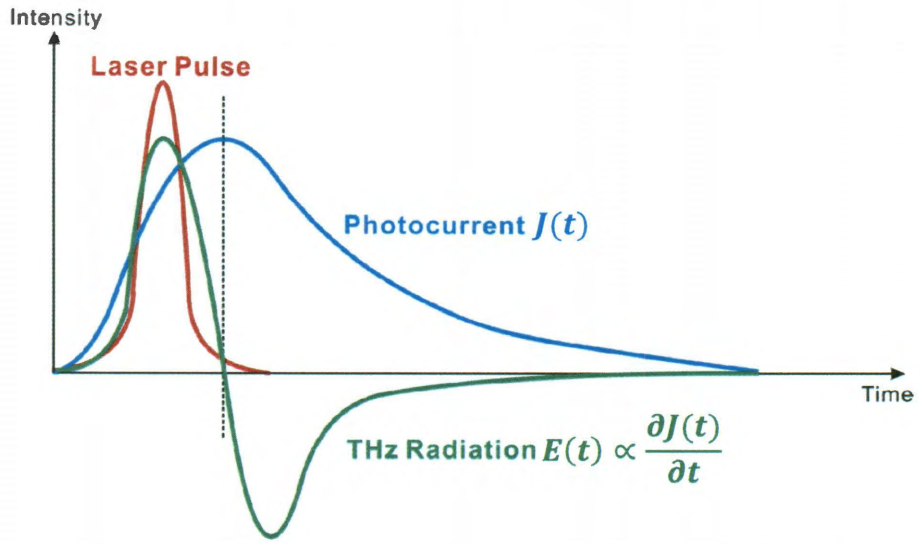

Figure 2.3 : The physical response of a voltage-biased photoconductive antenna to a focused femtosecond laser pulse: induced photocurrent by the focused optical pulse and radiated THz field according to Maxwell's equations.

An electromagnetic wave is radiated into free space from the transient photocurrent $J(t)$ according to Maxwell's equations, $E(t) \propto \partial J(t)/\partial t$. The radiated field is mainly dominated by the rising edge of the photocurrent. The response of the voltage-biased photoconductive antenna to an optical pulse focused onto the gap is illustrated in Fig. 2.3.

In our THz-TDS system, THz generation can be also obtained by the optical rectification process in the <110> ZnTe nonlinear crystal, as shown Fig. 2.4 [53]. Optical rectification contains a difference frequency mixing and occurs in media with large second order susceptibility $\chi^{(2)}$, which is a non-linear optical process consisting of the generation of a DC polarization and a second harmonic double-frequency item at the passage of an intense pulsed optical beam. For ultrashort laser pulses that have very large spectral bandwidth, the mixing of different frequency components produces

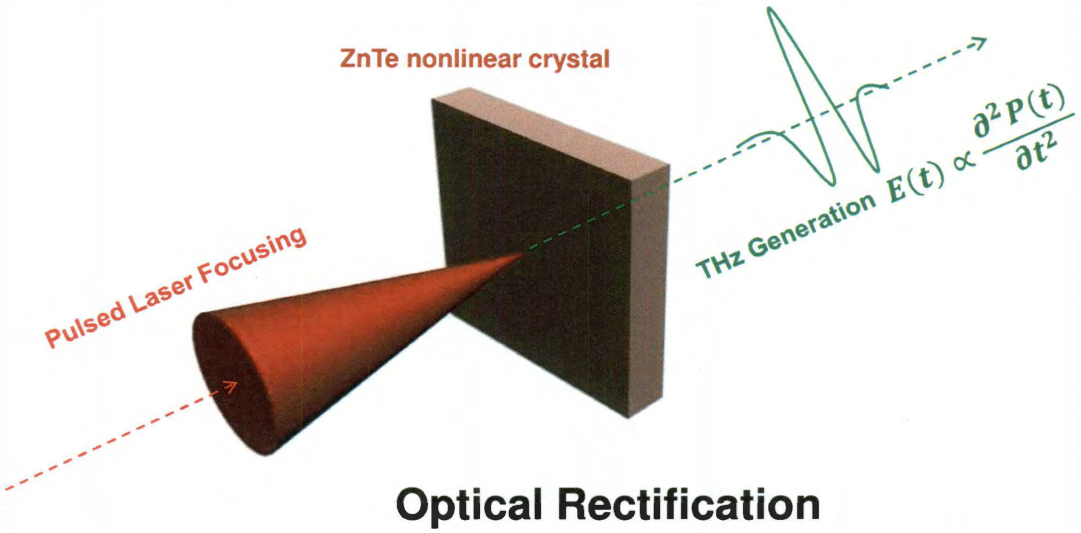

Figure 2.4 : Optical rectification for THz generation through a <110> ZnTe nonlinear crystal.

a beating polarization, which results in the emission of electromagnetic waves in the THz region.

2.2.2 THz Detector

The structure of the photoconductive antenna THz detector is exactly the same as that of the emitter shown in Fig. 2.2. The only difference is, when it is used for THz detection, we use a current ammeter (actually a current preamplifier in our experiment) to measure the photocurrent instead of applying a voltage (see Fig. 2.5). Again, a femtosecond laser pulse is focused onto the dipole center gap and generates photocarriers there. When it meets and overlaps with the THz pulse to be detected in the time domain, the electric field of the THz beam drives the photocarriers to the metal lines on the detector and forms a photocurrent, which is proportional to the amplitude of the received THz electric field. Through recording that photocurrent

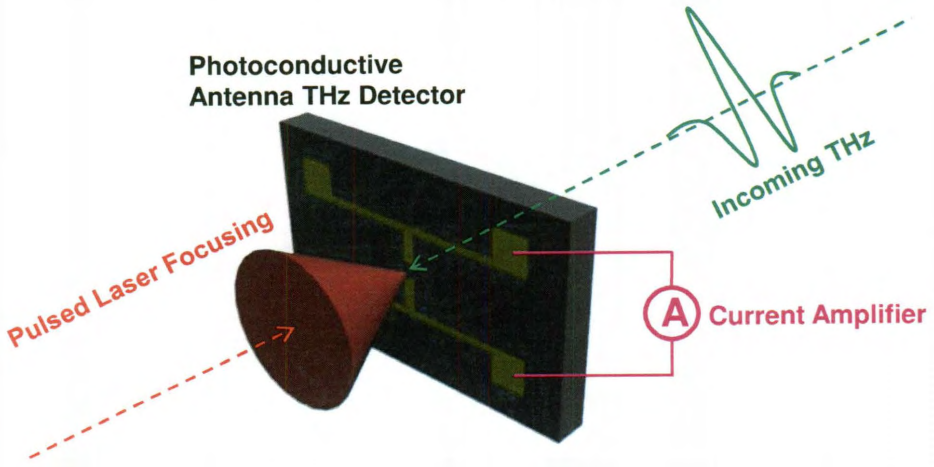

Figure 2.5 : THz detection process from photoconductive antenna detector.

value measured by the current ammeter, we equivalently record the THz electric field value at the corresponding temporal point. By changing the relative time-delay between the laser pulse and the THz pulse, the entire THz pulse can be mapped out in the time domain as shown in Fig. 2.6.

Finally, the mapped-out THz electric field value (in arbitrary units) as a function of relative time delay (usually in units of ps) forms the time domain data for THz-TDS, which can then be Fourier-transformed into the frequency domain to get both the amplitude spectrum and phase spectrum. For our THz-TDS system utilizing a ZnTe nonlinear crystal as the emitter and photoconductive antenna as the detector, typical time-domain data and the corresponding frequency-domain amplitude spectrum are shown in Figs. 2.7(a) and (b), respectively. It can be seen that, for such a THz-TDS system, the typical effective THz bandwidth is about 2.4 THz.

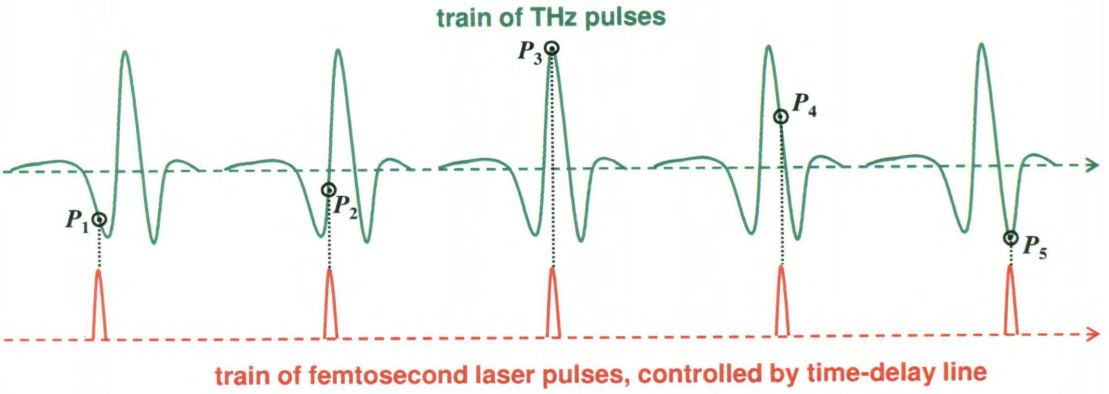

Figure 2.6 : THz waveform mapping through changing the relative time-delay between the probing laser pulse and the to-be probed THz pulse.

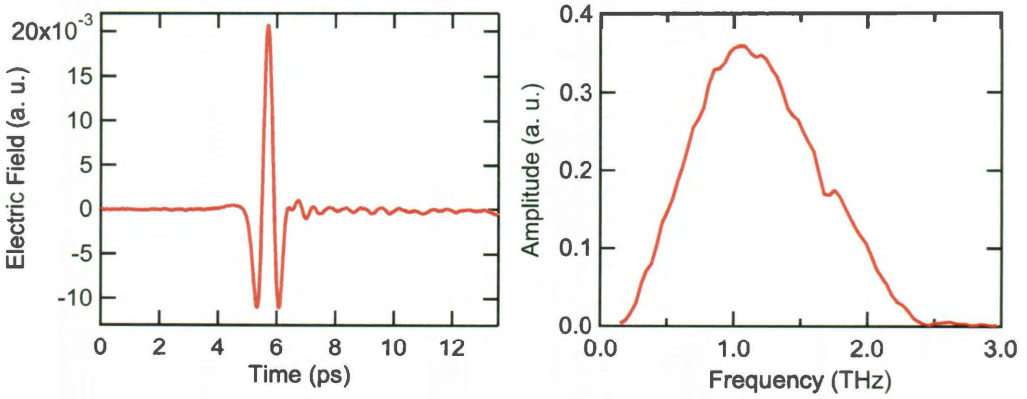

Figure 2.7 : Typical THz (a) waveform in the time-domain and (b) amplitude spectrum in the frequency domain.

2.3 Characterization of the THz-TDS System

Like all the measurement tools in physics, once the THz-TDS system is set up and its signal is obtained and fully optimized, the next job before formal measurements is to characterize it. In this section, we present two most important types of characterization for our THz-TDS system: profile and dynamics.

2.3.1 Gaussian beam profile tracing

Unlike spectroscopy work in the visible range, we cannot see THz radiation with our eyes, which makes THz measurements more complicated and challenging. We need to experimentally locate the THz beam focus and get its size, between the second and the third parabolic mirrors, and then we'll be able to make the film sample of the right size (larger than that of the THz beam focus) and locate it at the right position.

Since THz radiation cannot transmit through metals, the simplest profiling technique is the razor blade method [55]: a straight razor blade is shifting across the beam and the measured intensity is recorded at a series of points. Assuming that the THz beam is of a typical Gaussian shape, for an input total power intensity P, a measured power intensity p and a razor blade position x, we have the beam with waist w defined as:

$$x = -w/2, p = 0.84P; x = 0, p = 0.5P; x = w/2, p = 0.16P \tag{2.1}$$

Then, the intensity profile for this Gaussian beam can be expressed as:

$$I(x,y) = \frac{2P}{\pi w^2} e^{-\frac{2(x^2+y^2)}{w^2}}, \tag{2.2}$$

where I is the power intensity density, and y is the direction vertical to the razor blade across direction x.

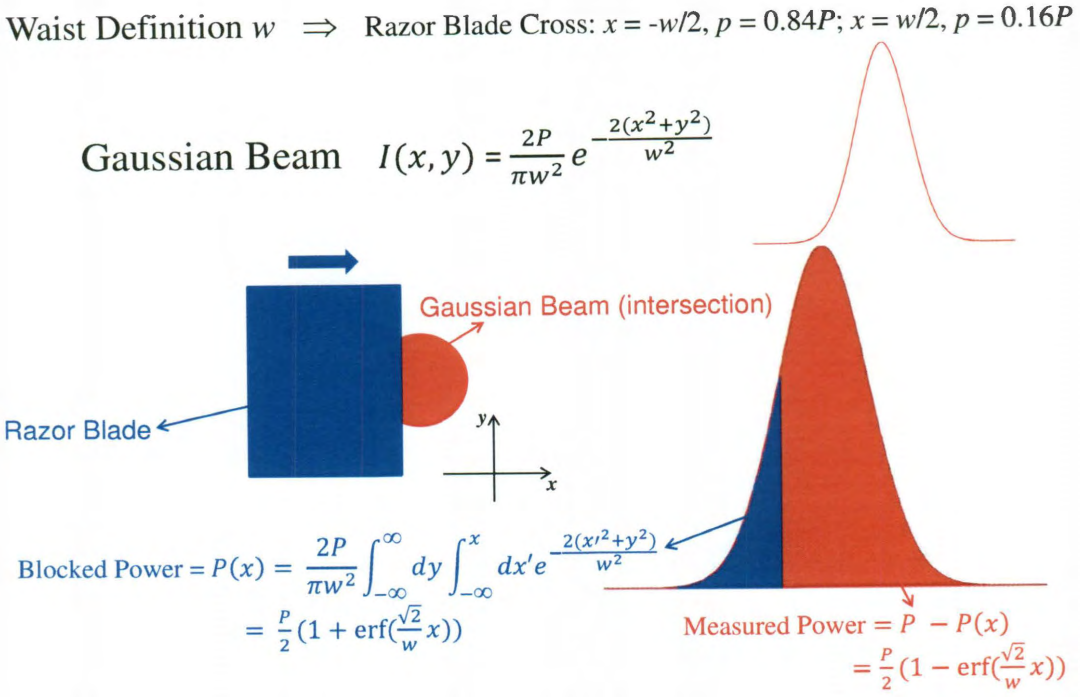

Figure 2.8 : Schematic illustration of the razor-blade method for Gaussian beam profile tracing, basically blue color represents for the "blocked" and red for the "unblocked".

As the razor blade crosses the THz Gaussian beam, the intensity of the power blocked by the razor can be calculated by the double integral:

$$P(x) = \frac{2P}{\pi w^2}\int_{-\infty}^{\infty} dy \int_{-\infty}^{x} dx' e^{-\frac{2(x'^2+y^2)}{w^2}} = \frac{P}{2}\left(1 + \mathrm{erf}\left(\frac{\sqrt{2}}{w}x\right)\right). \tag{2.3}$$

Then, the measured power intensity should finally be:

$$p(x) = P - P(x) = \frac{P}{2}\left(1 - \mathrm{erf}\left(\frac{\sqrt{2}}{w}x\right)\right) \tag{2.4}$$

The entire process of this method is illustrated in Fig. 2.8, where blue areas represent the "blocked" areas and red the "unblocked" areas.

Thus, we measured the transmitted THz beam power intensity $p(x)$ as a function of the razor blade cross position x in the middle between the second and the third

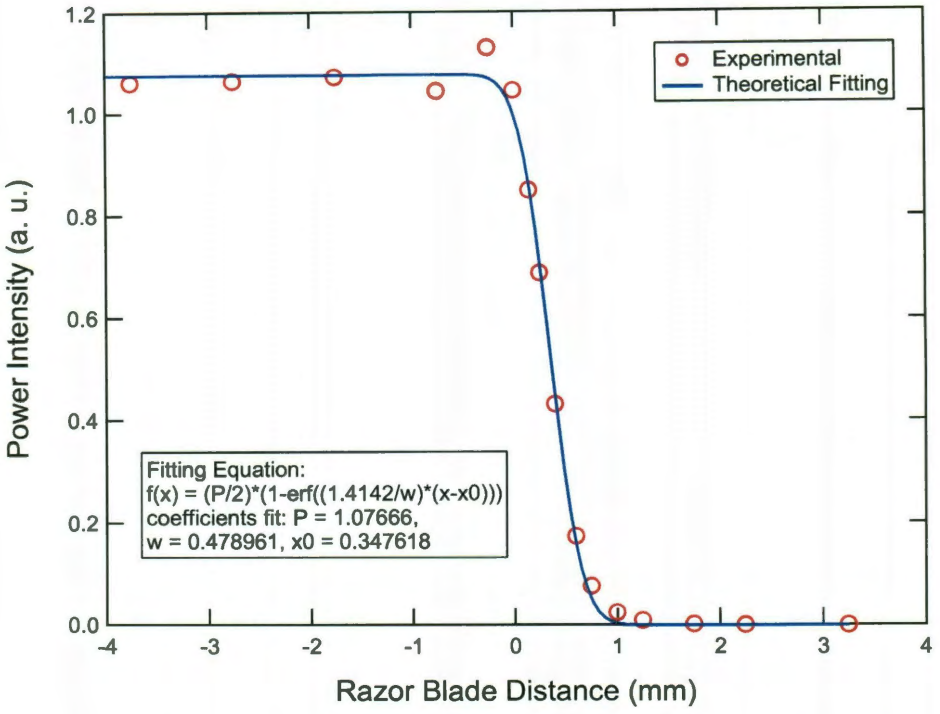

Figure 2.9 : Gaussian beam profiling result via razor-blade method, with red circles for experimental data and blue line for theoretical fitting.

parabolic mirrors. Theoretical fitting with Eq. (2.4) would give us the beam waist value w. The results are shown in Fig. 2.9, in which we can see that the experimental data (red circles) fits well with Eq. (2.4) (blue line). This also further confirms the Gaussian shape of the THz beam. The obtained waist value $w = 0.48$ mm, which indicates the THz beam diameter at the focus is $2w \sim 1$ mm. However, this is just the waist, the central part of the Gaussian beam. In order not to lose the information at the two Gaussian edges, a film sample size of at least ~ 4 mm $\times$ 4 mm is still suggested.

2.3.2 Standard sample measurement – n-type silicon wafer

For decades physicists have studied the dynamics of carriers in semiconductors. Here, we choose a standard n-type silicon wafter, whose carrier dynamics are well known and describable by the Drude model, to characterize our THz-TDS system.

The silicon wafer sample was purchased from POLISHED PRIME WAFERS in 2003. It is phosphorus-doped n-type silicon, with a thickness of $\sim$ 520 μm and an crystalline orientation of (100). Its documented resistivity range is 0.5 – 1.0 Ωcm.

This subsection shows our THz-TDS measurements of n-type silicon. First, we need to establish right models and equations to quantitatively describe the interaction process between the THz wave and silicon wafer with thickness d, as shown in Fig. 2.10. $\tilde{E}_s(\omega)$ and $\tilde{E}_r(\omega)$ are the complex signals in the frequency domain for the transmitted THz waves through the silicon wafter sample and the air as a reference, respectively, and $\tilde{E}_i(\omega)$ is that for the incoming THz wave. In order to avoid water absorption in humid air, we installed a nitrogen purging box that covers the whole system and makes the experiment running under slow dry N_2 flow, which will be shown in detail in Chapter 4. Here, for simplicity we still use "Air" instead of "N_2" to avoid any confusions. 0 and 1 denote the air reference and the silicon sample, respectively, and c is the speed of light in free space.

Considering the silicon wafer as a thick medium, we have the following expression for the sample signal

$$\tilde{E}_s(\omega) = \tilde{E}_i(\omega)\tilde{t}_{01}\exp\left[-i\frac{\omega d}{c}\tilde{n}(\omega)\right]\tilde{t}_{10} \tag{2.5}$$

and

$$\tilde{E}_r(\omega) = \tilde{E}_i(\omega)\exp\left(-i\frac{\omega d}{c}\right) \tag{2.6}$$

for the reference signal, respectively, based on the assumption that $n_0 = 1$ for air.

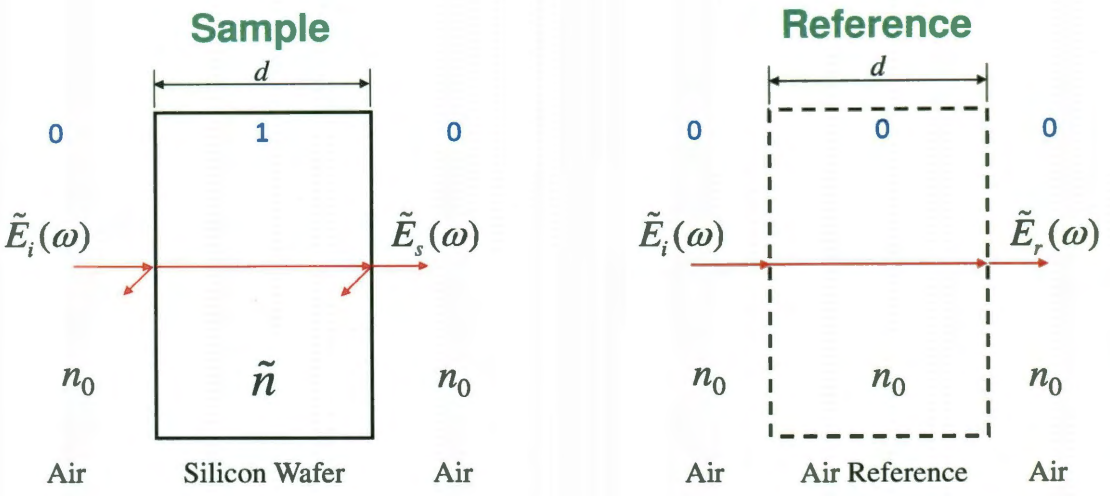

Figure 2.10 : Transmission analysis diagram for the thick medium silicon wafer.

Finally, the equation to solve for the complex refractive index $\tilde{n}(\omega)$ of the silicon wafer is derived as

$$\tilde{T}(\omega) = \frac{\tilde{E}_s(\omega)}{\tilde{E}_r(\omega)} = \tilde{t}_{01}\tilde{t}_{10}\exp\left[-i\frac{\omega d}{c}(\tilde{n}(\omega)-1)\right] = \frac{4\tilde{n}(\omega)}{(\tilde{n}(\omega)+1)^2}\exp\left[-i\frac{\omega d}{c}(\tilde{n}(\omega)-1)\right] \tag{2.7}$$

by plugging in the Fresnel's relations

$$\tilde{t}_{10} = \frac{2\tilde{n}_1}{n_0+\tilde{n}_1} = \frac{2\tilde{n}(\omega)}{1+\tilde{n}(\omega)}, \tilde{t}_{01} = \frac{2n_0}{\tilde{n}_1+n_0} = \frac{2}{\tilde{n}(\omega)+1}. \tag{2.8}$$

Afterwards, once we have $\tilde{n}(\omega)$, we could further obtain the complex dielectric function $\tilde{\varepsilon}(\omega)$ and then the complex conductivity $\tilde{\sigma}(\omega)$ through the Eq. (1.4) in Chapter 1 when we introduce the optical conductivity:

$$\tilde{n}(\omega)^2 = \tilde{\varepsilon}(\omega) = \varepsilon_{Si} - i\frac{\tilde{\sigma}(\omega)}{\omega\varepsilon_0}, \tag{2.9}$$

where $\varepsilon_0 = 8.85 \times 10^{-12}$ Fm^{-1} is the permittivity of free space and $\varepsilon_{Si} = 11.7$ is the static intrinsic silicon dielectric constant.

Note the "−" sign before "i". This depends on how one defines other quantities. Based this convention, we also have the dynamic refractive index, dielectric function and conductivity expressed as $\tilde{n}(\omega) = N(\omega) - i\kappa(\omega)$, $\tilde{\varepsilon}(\omega) = \varepsilon'(\omega) - i\varepsilon''(\omega)$, and $\tilde{\sigma}(\omega) = \sigma'(\omega) - i\sigma''(\omega)$, respectively, same as those defined in §1.3 except the opposite signs in the middles.

Figure 2.11 shows the transmitted time-domain THz waveforms with (red) and without (blue) the n-type silicon sample. We see a large time delay between them because of the phase dispersion caused by the finite refractive index of silicon. In addition, there is a huge attenuation for the wave due to the absorption caused by an appreciable amount of free carriers in the phosphorus-doped silicon.

The corresponding frequency-domain data could be obtained by a direct fast Fourier transform (FFT) of the time-domain data above, and the resulted amplitude spectrum ($|\tilde{E}_s(\omega)|$ and $|\tilde{E}_r(\omega)|$) is shown in Fig. 2.12(a), where we can see the large absorption. The resulted phase spectrum (Phase($\tilde{E}_s(\omega)$) and Phase($\tilde{E}_r(\omega)$)) is illustrated in Fig. 2.12(b), in which the dispersion is clearly demonstrated.

Now, since we have both $\tilde{E}_s(\omega)$ and $\tilde{E}_r(\omega)$, from Eq. (2.7) we should be able to obtain $\tilde{n}(\omega)$ directly. Using a Matlab program, we solved the complex refractive index $\tilde{n}(\omega)$ and plotted its real and imaginary parts in Figs. 2.13(a) and (b), respectively. Afterwards, a further calculation through Eq. (2.9) provided both the real and imaginary parts of the dynamic conductivity $\tilde{\sigma}(\omega)$, which are shown in Figs. 2.13(c) and (d), respectively.

All these experimental data are depicted as blue circles, while the green solid lines are their corresponding theoretical fits with the Drude model

$$\tilde{\sigma}(\omega) = \frac{\sigma_0}{1 - i\omega\tau} \tag{2.10}$$

where σ_0 is the DC conductivity and τ is the carrier scattering time. As we can see

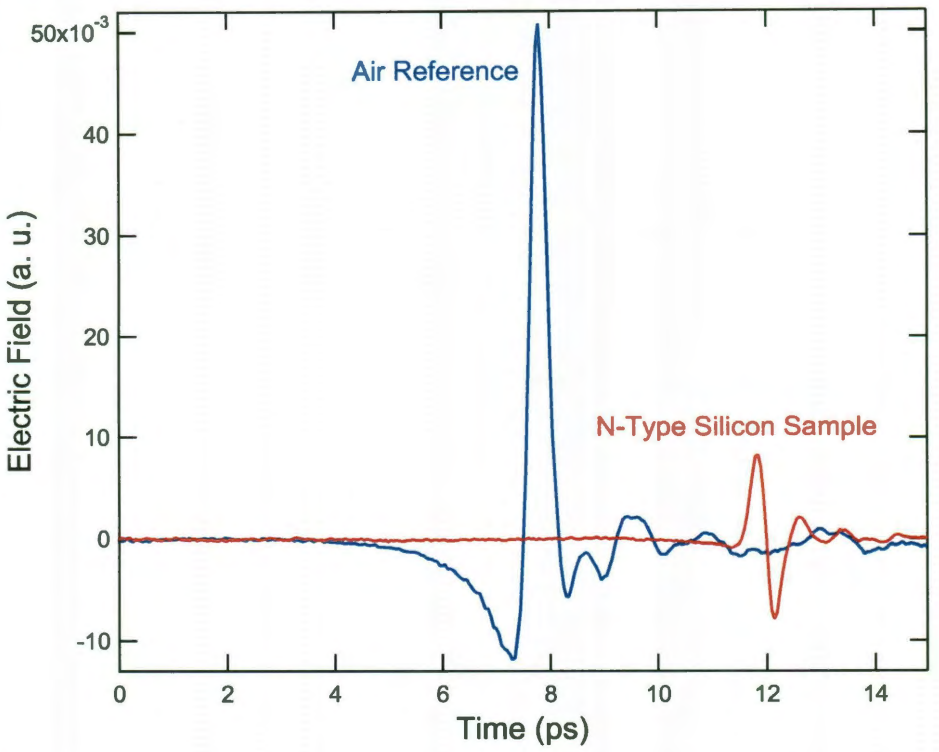

Figure 2.11 : Time-domain THz waveforms transmitted through the n-type silicon sample (red) and air reference (blue).

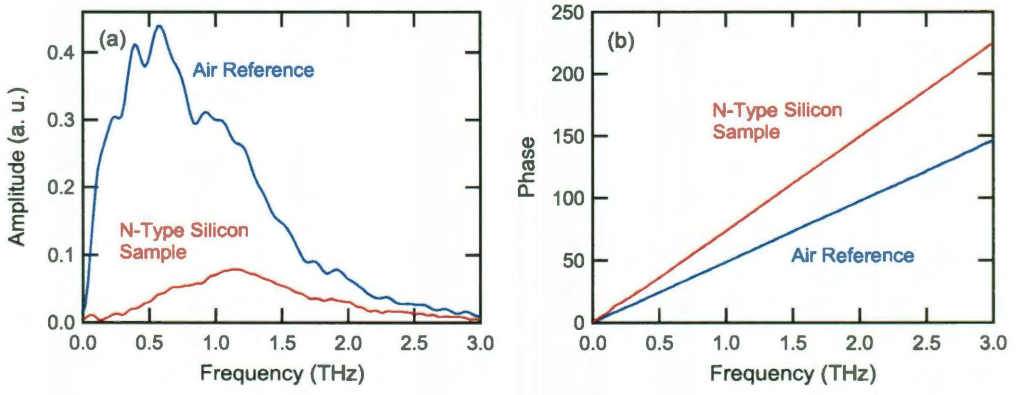

Figure 2.12 : Frequency domain spectra of the n-type silicon sample (red) and air reference (blue): (a) amplitude spectrum, and (b) phase spectrum

from these figures, all of them fit with the Drude model very well, except for some small deviations in the low frequency parts of the real refractive index and imaginary conductivity.

The dynamic conductivity $\sigma(\omega)$ is the most basic quantity for discussing electron motions. As Figs. 2.13(c) and (d) show, the observed strong frequency dependence of the real and imaginary conductivities is due to the free carriers, not any types of phonons. The real part of the conductivity drops from its DC value to a reduced value at the highest measured frequency of 1.8 THz, while the imaginary part of the conductivity increases from zero at low frequencies, peaks in the mid-range, and then shows a gradual decline. They both obey the Drude model [Eq. (2.10)] well, which describes a classical gas of non-interacting electrons usually in metals and semiconductors. The obtained DC conductivity values are $\sigma_0 = 1.02$ S/cm from the real conductivity and 1.16 S/cm from the imaginary conductivity, and the obtained carrier scattering time values are $\tau = 2.06 \times 10^{-13}$ sec from the real conductivity and 1.74×10^{-13} sec from the imaginary conductivity. Therefore, the two independent Drude fittings for real and imaginary conductivities have a reasonable agreement. Also, the obtained DC conductivity value agrees very well with the documented data ($0.5 - 1.0$ Ωcm) for this silicon product.

2.4 Advantages of THz-TDS

THz-TDS now has been widely used for studying the optical conductivities of all kinds of solid films and proven to be a very powerful technique. It has several exceptional advantages [56].

A high signal-to-noise ratio of $\sim 10^6$ can be achieved in THz-TDS due to its use of gated detection. The THz detector is in OFF status for most of the time between

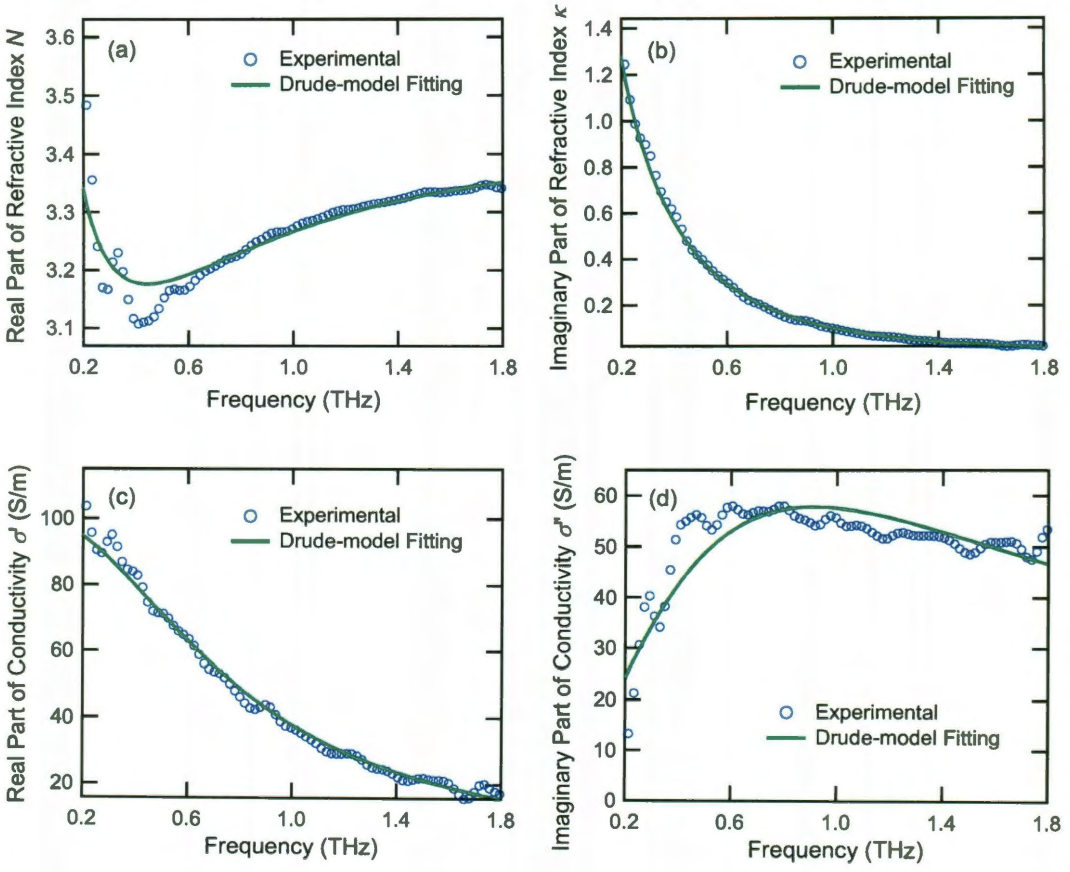

Figure 2.13 : THz dynamics of the n-type silicon sample: (a) real part of refractive index, (b) imaginary part of refractive index, (c) real part of conductivity, and (d) imaginary part of conductivity

THz pulses, and hence its resistance is always high between laser pulses and Johnson noise (thermal noise) can be almost negligible.

As we mentioned once in the last paragraph of Chapter 1 when we were introducing optical conductivity, THz-TDS offers a direct measurement of the electric field $E(t)$ of the THz electromagnetic wave instead of just its power intensity. Thus, both amplitude and phase information can be obtained. Then, both the real and imaginary parts of the material dielectric function can be extracted through their interactions without using the lengthy and somehow uncertain Kramers-Kronig analysis. This is a crucial advantage compared with conventional Fourier transform infrared (FTIR) spectroscopy, in which only power intensity spectra could be measured and afterwards only the amplitude change information could be recorded while phase information being lost.

Because in THz-TDS the wave signal is detected in the time domain, dynamic features in condensed matter physics such as coherent phenomena and carrier dynamics can be studied directly without using Fourier transformation.

Very significantly for our project, THz-TDS provides us with a conductivity measurement method without the presence of those metal contacts, which will definitely induce the unwanted additional resistance. Also, this kind of conductivity measurement possesses a great experimental flexibility and can be developed for studying both simple (or homogeneous) and complex (inhomogeneous) systems, and the conductivity itself can be measured as a function of optical frequency, temperature, magnetic field, electric field, orientation, ...

Chapter 3

Physics of Low-Dimensional Carbon Nanomaterials

Nanostructured carbon materials include a wide range of systems, such as fullerenes, single-walled carbon nanotubes (SWNTs), multi-walled carbon nanotubes (MWNTs), nano-diamonds, fibers, scrolls, cones, whiskers, and graphene. The carbon nanomaterials that we focus on in this thesis are SWNTs and graphene, two low-dimensional sp^2-bonded carbon nanostructures that have been attracting much attention in recent years.

3.1 Crystal and Electronic Energy-Band Structure

3.1.1 Graphene

A SWNT is a rolled-up version of single-layer graphene, and thus, we introduce the crystal and energy-band structure of graphene first. Graphene consists of a single layer of carbon atoms arranged into a two-dimensional (2D) hexagonal structure, as shown in Fig. 3.1(a). The crystalline structure of graphene can be seen as a triangular lattice with a basis of two atoms (denoted as A and B) per unit cell, as shown in Fig. 3.1(b). The lattice vectors can be represented as

$$\boldsymbol{a}_1 = \frac{a}{2}(3, \sqrt{3}), \boldsymbol{a}_2 = \frac{a}{2}(3, -\sqrt{3}) \tag{3.1}$$

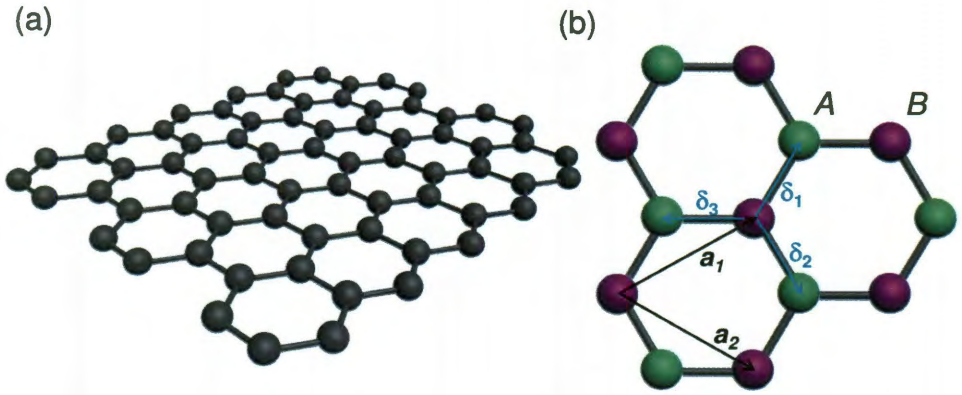

Figure 3.1 : (a) Graphene (b) Crystalline lattice structure of graphene, $\boldsymbol{a_1}$ and $\boldsymbol{a_2}$ are the lattice unit vectors, and δ_i, $i = 1, 2, 3$ are the nearest neighbor vectors.

where $a \approx 1.42$ $\mathring{A}$ is the carbon-carbon distance. The reciprocal lattice unit vectors can then be given by

$$\boldsymbol{b_1} = \frac{2\pi}{3a}(1, \sqrt{3}), \boldsymbol{b_2} = \frac{2\pi}{3a}(1, -\sqrt{3}). \tag{3.2}$$

In k-space, the two points at the corners of the first Brillouin zone, $\boldsymbol{K}$ and $\boldsymbol{K'}$, are of particular importance for the physical properties of graphene, and they are named Dirac points for the reason which will be explained later. Their positions in momentum space are given by the following equation and depicted in Fig. 3.2 [57].

$$\boldsymbol{K} = \left(\frac{2\pi}{3a}, \frac{2\pi}{3\sqrt{3}a}\right), \boldsymbol{K'} = \left(\frac{2\pi}{3a}, -\frac{2\pi}{3\sqrt{3}a}\right) \tag{3.3}$$

Let us look at Fig. 3.1(b) again. The three nearest neighbor vectors in real space are given by

$$\boldsymbol{\delta}_1 = \frac{a}{2}(1, \sqrt{3}), \boldsymbol{\delta}_2 = \frac{a}{2}(1, -\sqrt{3}), \boldsymbol{\delta}_3 = -a(1, 0) \tag{3.4}$$

while the six second nearest neighbors are located at:

$$\boldsymbol{\delta'}_1 = \pm\boldsymbol{a}_1, \boldsymbol{\delta'}_2 = \pm\boldsymbol{a}_2, \boldsymbol{\delta'}_3 = \pm(\boldsymbol{a}_2 - \boldsymbol{a}_1) \tag{3.5}$$

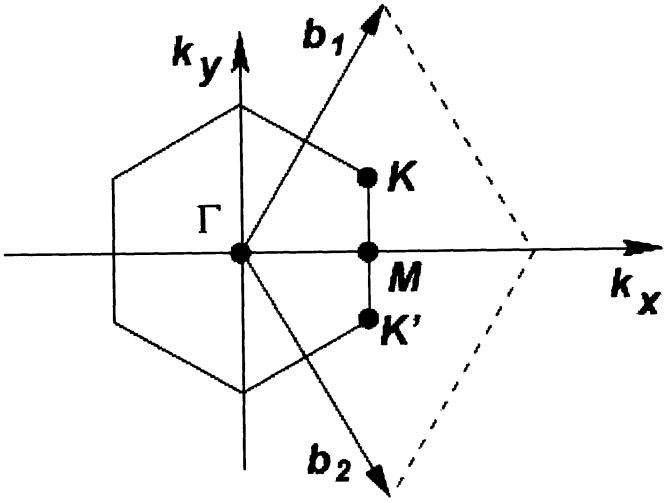

Figure 3.2 : Brillouin zone. The Dirac points are located at the $\boldsymbol{K}$ and $\boldsymbol{K'}$ points. Reproduced from Ref. [57].

Using the nearest-neighbor tight-binding approximation, the Hamiltonian for electrons in graphene has the following form (a unit system used for $\hbar = 1$):

$$H = -t \sum_{<i,j>,\sigma} (a^{\dagger}_{\sigma,i} b_{\sigma,j} + \text{h.c.}) - t' \sum_{<<i,j>>,\sigma} (a^{\dagger}_{\sigma,i} a_{\sigma,j} + b^{\dagger}_{\sigma,i} b_{\sigma,j} + \text{h.c.}) \qquad (3.6)$$

where $a_{i,\sigma}$ and $a^{\dagger}{}_{i,\sigma}$ denote an annihilation and a creation of an electron with spin σ ($\sigma = \uparrow\downarrow$) on site $\mathbf{R}_i$ on sublattice A (an equivalent definition is used for sublattice B), respectively, t ($\approx$ 2.8 eV) is the nearest neighbor hopping energy (hopping between different sublattices, such as A $\rightleftharpoons$ B), and t' is the next nearest neighbor hopping energy (hopping between the same sublattices, such as A $\rightarrow$ A and B $\rightarrow$ B). Then, the electron energy bands derived from this Hamiltonian have the following form (Ref. [58]):

$$E_{\pm}(\mathrm{k}) = \pm t\sqrt{3 + f(\mathrm{k})} - t' f(\mathrm{k}), f(\mathrm{k}) = 2\cos(\sqrt{3}k_y a) + 4\cos(\frac{\sqrt{3}}{2}k_y a)\cos(\frac{3}{2}k_x a) \qquad (3.7)$$

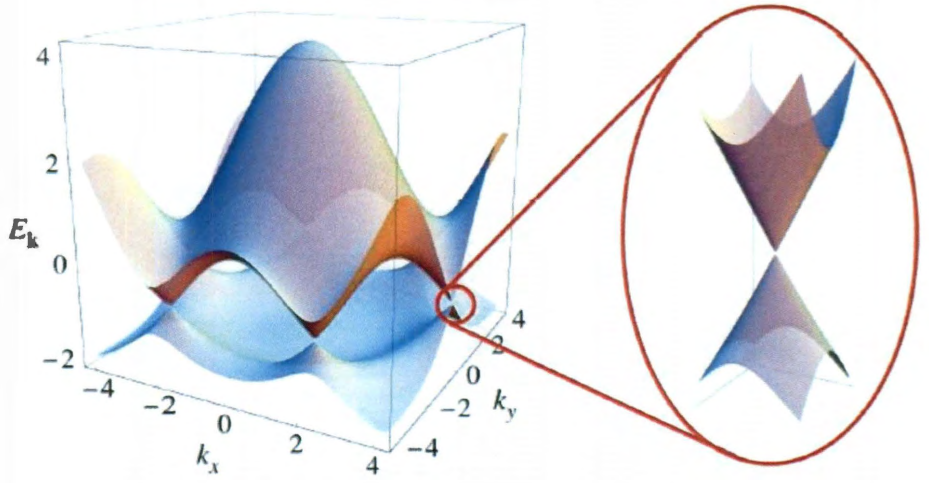

Figure 3.3 : Electron energy band of graphene obtained under tight-binding approximation, with $t = 2.7$ eV and $t' = 0.2t$. Energy is in unit of t. Right: zoom-in of the energy bands around one of the Dirac points. Reproduced from Ref. [57].

where the + sign refers to the upper (π, conduction) band and the − sign applies to the lower (π^*, valence) band. From the above equation, we can clearly see that the energy spectrum is symmetric around the zero energy if $t' = 0$. For a finite value of t', that symmetry between conduction band and valence band is broken. A full energy bandstructure of graphene including both t and t' is shown in Fig. 3.3, together with a zoom-in inset around one of the Dirac points ($\boldsymbol{K}$ or $\boldsymbol{K'}$ point at Brillouin zone, as we mentioned above) [57].

The significant energy dispersion relation could be obtained by expanding the entire bandstructure in Eq. (3.7) close to the $\boldsymbol{K}$ (or $\boldsymbol{K'}$) vector shown in Eq. (3.3) as $\mathbf{k} = \boldsymbol{K} + \mathbf{q}$ with $|\mathbf{q}| \ll |\boldsymbol{K}|$ (Ref. [58]):

$$E_{\pm}(\mathbf{q}) \approx \pm v_F |\mathbf{q}| + O((q/K)^2) \tag{3.8}$$

where $\mathbf{q}$ is the momentum measured relatively to the Dirac points and v_F stands for

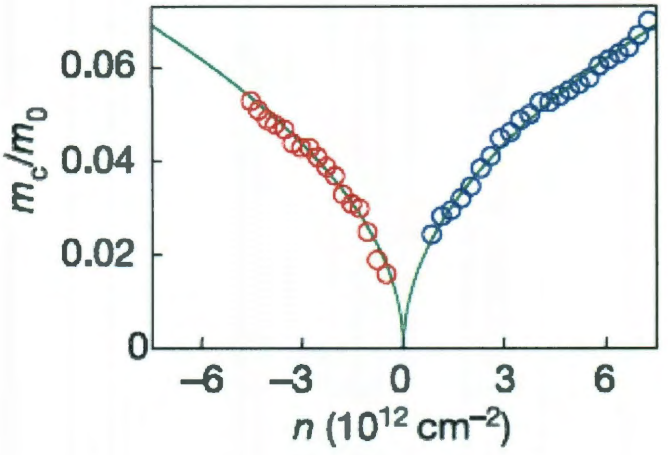

Figure 3.4 : Cyclotron mass of charge carriers in graphene as a function of their concentration n. Positive and negative n correspond to electrons and holes, respectively. Reproduced from Ref. [36].

the Fermi velocity, given by $v_F = 3ta/2$, with a value $v_F \simeq 1 \times 10^6$ m/s. This result was first reported by Wallace [58].

Strikingly, this energy dispersion spectrum clearly shows a linear relation, in marked contrast to conventional systems with parabolic relation $E(\mathbf{q}) = q^2/(2m)$ where m is the effective mass. This photon-like, linear dispersion describes ultra-relativistic particles, which obey the Dirac equation instead of the Schrödinger equation. Also, from Eq. (3.8) a cyclotron mass is derived as

$$m^* = \frac{\sqrt{\pi}}{v_F}\sqrt{n} \tag{3.9}$$

where n is the electron density. An experimental demonstration of this was made by Novoselov *et al.* in 2005 [36] and is shown in Fig. 3.4, which provides evidence of massless Dirac fermions (DFs) in graphene.

3.1.2 Single-Walled Carbon Nanotubes

An in-depth scanning tunneling microscopy (STM) study of SWNTs confirmed that the SWNT is derived from the 2D graphene sheet by rolling it up into a cylinder [59], as shown in Fig. 3.5. Therefore, the structure of a SWNT can be easily defined based on that of graphene through a so-called chiral vector $\boldsymbol{C}_h = n\boldsymbol{a}_1 + m\boldsymbol{a}_2$, where $\boldsymbol{a}_1$ and $\boldsymbol{a}_2$ are the unit vectors of the graphene structure shown in Eq. (3.1), and n and m are integers, as shown in Fig. 3.6(a). $\boldsymbol{C}_h$ connects two equivalent points on the 2D graphene sheet, like point O and point A. It determines the construction of the nanotube, depending uniquely on the integer pair (n, m), or chirality. The angle θ between the chiral vector $\boldsymbol{C}_h$ and the "zigzag" direction ($\theta = 0$) is called the chiral angle. The intersection of $\boldsymbol{C}_h$ (which is normal to it), $\overrightarrow{OB}$, with the first lattice point, determines the basic one-dimensional (1D) translation vector $\boldsymbol{T}$, which can be defined as $\boldsymbol{T} = t_1\boldsymbol{a}_1 + t_2\boldsymbol{a}_2$ with the indices $t_1 = (2m + n)/d_r$ and $t_2 = (m + 2n)/d_r$ where d_r is the greatest commmon denominator of $2m + n$ and $m + 2n$. The unit cell of SWNT is then the rectangle defined by the vectors $\boldsymbol{C}_h$ and $\boldsymbol{T}$. The nanotube is formed through rolling up the unit cell by superimposing the two ends of the chiral vector $\boldsymbol{C}_h$ (O and A). Then, the diameter and chiral angle of the SWNT can be calculated as the following equations, respectively:

$$d_t = \frac{C_h}{\pi} = \frac{\sqrt{3}a(m^2 + mn + n^2)^{\frac{1}{2}}}{\pi} \tag{3.10}$$

and

$$\theta = \tan^{-1}[\sqrt{3}n/(2m + n)] \tag{3.11}$$

Here we can see that the chirality (n, m) solely describes the way how nanotube is formed from graphene.

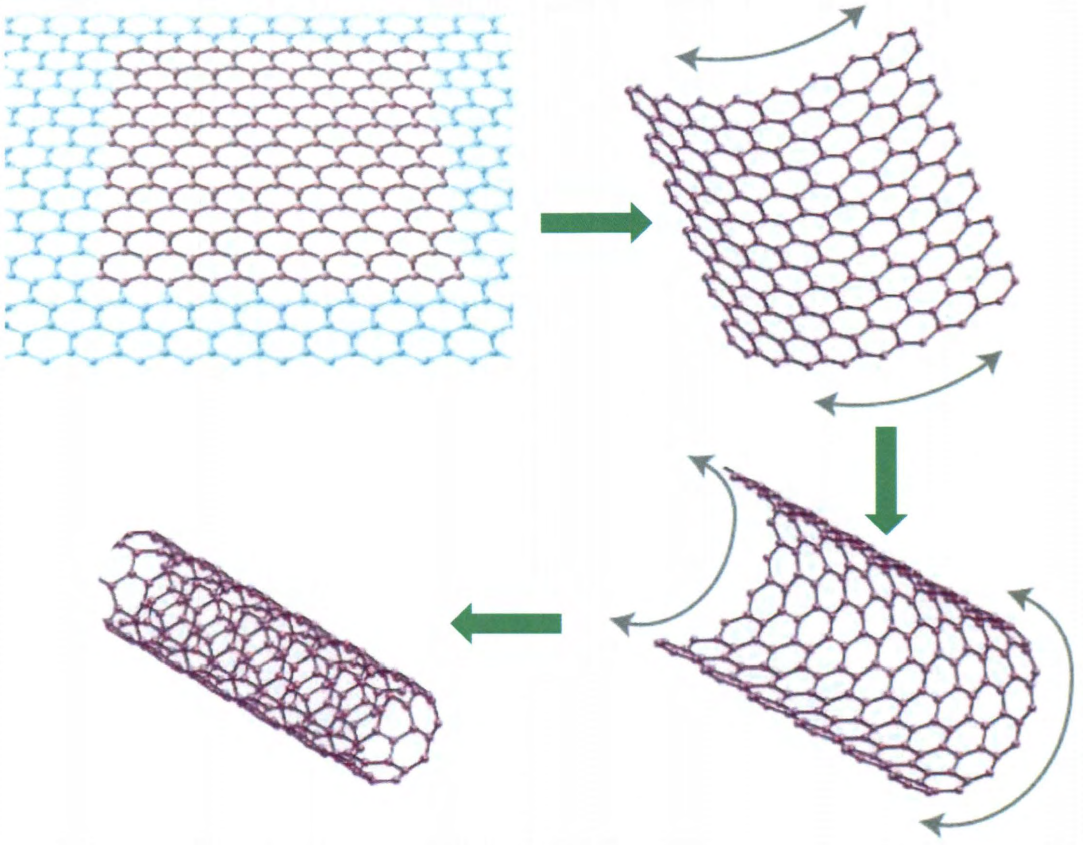

Figure 3.5 : Single-walled carbon nanotube is built by rolling up a single-layer 2D graphene sheet. Adapted from Ref. [35].

.

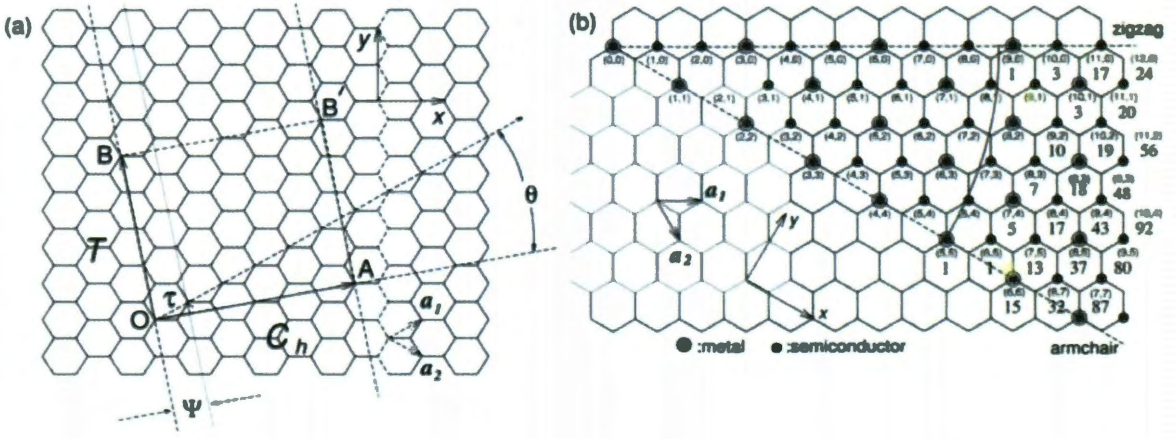

Figure 3.6 : (a)The geometry of how 2D graphene sheet is rolled up to SWNT, and the definitions of different chirality quantities. (b) The relation between chiralities (n, m)s and the SWNTs species. Reproduced from Ref. [60]

.

The real space crystalline structure of SWNT determines its electronic energy bandstructure. Since as it is shown above, SWNT is a rolled sheet of graphene, its bandstructure is closely related to that of graphene given by Eq. (3.7) and Eq. (3.8). We start from the linear dispersion of graphene near the $\boldsymbol{K}$ or $\boldsymbol{K'}$ point:

$$E^{\pm}_{g2D}(|\vec{k}_{2D}|) = \pm\frac{\sqrt{3}}{2}\gamma_0|\vec{k}_{2D}|a \tag{3.12}$$

where γ_0 is the carbon-carbon transfer energy ($\sim$ 3 eV) and $|\vec{k}_{2D}| = 0$ at the $\boldsymbol{K}$ point. The way the nanotube is rolled requires a circumferential boundary condition on the planar wave, together with the Bloch theory, to be:

$$\psi_{n\vec{k}}(\vec{r} + \vec{C_h}) = e^{i\vec{k}\cdot\vec{C_h}}\psi_{n\vec{k}}(\vec{r}). \tag{3.13}$$

To ensure during the SWNT rolling the edge state of one side is superimposed exactly with that of the other, $\vec{k}_{2D}\cdot\vec{C_h} = 2\pi j$ needs to be met, where j is an integer.

All these conditions would produce the 1D dispersion relations of SWNT as:

$$E_{\mu}^{\pm}(k) = E_{g2D}^{\pm}(k\frac{\boldsymbol{K}_2}{|\boldsymbol{K}_2|} + \mu\boldsymbol{K}_1), (-\frac{\pi}{T} < k < \frac{\pi}{T}, \mu = 1, \cdots, N) \tag{3.14}$$

where T is the magnitude of the translational vector $\boldsymbol{T}$, k is the 1D wave vector along the nanotube axis, and N denotes the number of hexagons of the graphene honeycomb lattice within the nanotube unit cell (see Fig. 3.6 (a)). T and N are given, respectively, by

$$T = \frac{\sqrt{3}C_h}{d_R} = \frac{\sqrt{3}\pi d_t}{d_R} \tag{3.15}$$

and

$$N = \frac{2(n^2 + m^2 + nm)}{d_R} \tag{3.16}$$

where d_R is the greatest common divisor of $(2n + m)$ and $(2m + n)$.

Very importantly, $\boldsymbol{K}_1$ and $\boldsymbol{K}_2$ represent, respectively, a discrete unit wave vector along the circumferential direction, and a reciprocal lattice vector along the nanotube axis direction, and are given by

$$\boldsymbol{K}_1 = [(2n + m)\boldsymbol{b}_1 + (2m + n)\boldsymbol{b}_2]/Nd_R, \boldsymbol{K}_2 = (m\boldsymbol{b}_1 - n\boldsymbol{b}_2)/N \tag{3.17}$$

where $\boldsymbol{b}_1$ and $\boldsymbol{b}_2$ are the reciprocal lattice vectors for graphene given by Eq. (3.2). These effectively "cut" the 2D Brillouin Zone (BZ) of graphene along lines of $k\boldsymbol{K}_2/|\boldsymbol{K}_2|$ $+ \mu\boldsymbol{K}_1$. In Fig. 3.7, several cutting lines near one of the K points are shown. The distance between two adjacent lines and the length of the cutting lines are given by the $\boldsymbol{K}_1$ and $\boldsymbol{K}_2$ vectors in Eq. (3.17), respectively, and their lengths are given by

$$|\boldsymbol{K}_1| = \frac{2}{d_t}, |\boldsymbol{K}_2| = \frac{2\pi}{T} = \frac{2d_R}{\sqrt{3}d_t} \tag{3.18}$$

For a particular nanotube with chirality of (n, m), if a cutting line passes through the K point of the 2D Brillouin Zone, as shown in Fig. 3.7 (a), where the π conduction

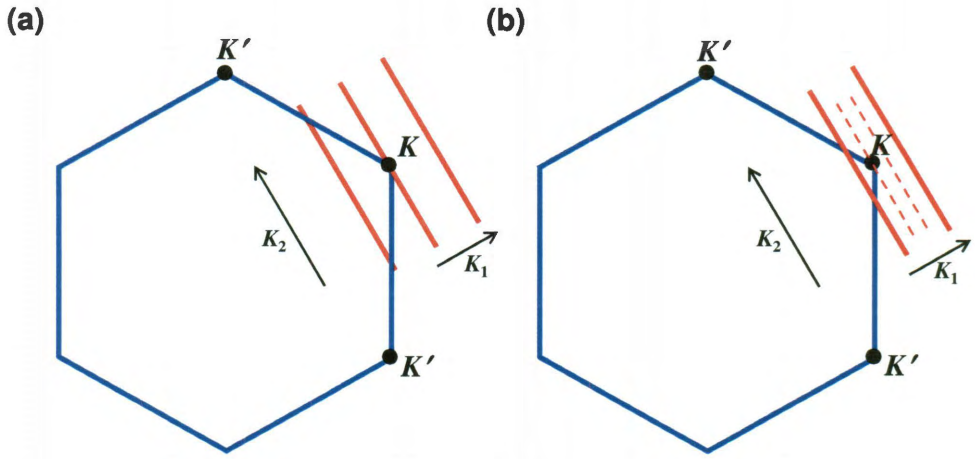

Figure 3.7 : The hexagons in blue lines are 2D graphene Brillouin zones. The wave vector k for 1D SWNT as red lines for (a) metallic and (b) semiconducting SWNTs. In the direction of $\boldsymbol{K}_1$, discrete k values are obtained by periodic boundary conditions for the SWNT circumferential direction. (a) For metallic SWNT, red line intersects a K point at the Fermi level of graphene. (b) For semiconducting SWNT, the K point always stands one-third of the distance between two red lines.

band and the π^* valence band of graphene touches each other, then the 1D energy band of SWNT has a zero band gap. Because that degenerate Dirac point lies on the Fermi level, the density of states are finite and hence the SWNT is metallic. On the other hand, if the K point is sitting between two cutting lines (always located in positions one-third of the distance between two adjacent cutting lines, as Fig. 3.7 (b) shown), the SWNT is semiconducting with a finite band gap and a zero density of states at the Fermi level. Then, the criterion for metallic and semiconducting SWNT is derived as $(n - m) \bmod 3 = 0$ and $(n - m) \bmod 3 = 1$ or 2, respectively [19, 61]. In special cases, when $n = m$ (then $\theta = 30°$), it is called an armchair nanotube; when $m = 0$ (then $\theta = 0°$), it is called a zigzag nanotube. The relation between SWNT's chiral geometry and its metallicity is summarized in Fig. 3.6(b).

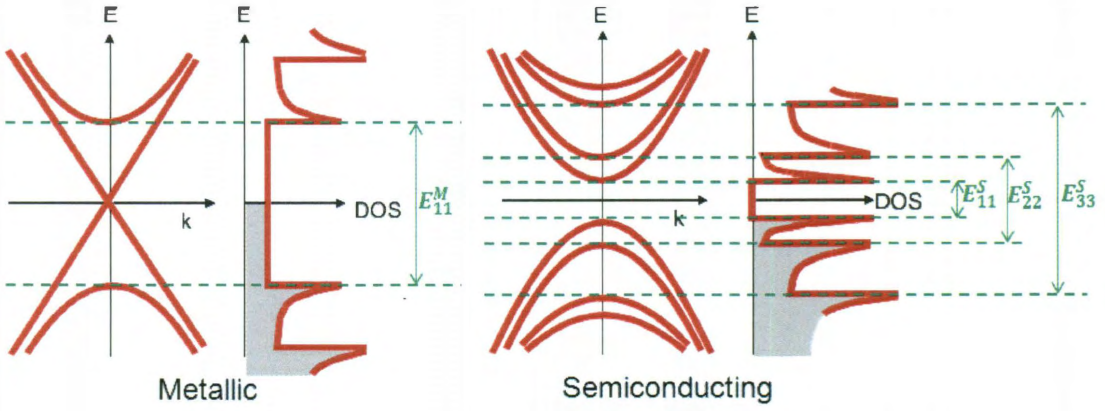

Figure 3.8 : 1D density of states for metallic (left) and semiconducting (right) SWNT, together with their electronic energy bandstructures, and several most common optical transitions between van Hove singularity subbands: E_{11}^M, E_{11}^S, E_{22}^S, and E_{33}^S

The 1D density of states (DOS) in units of states/C-atom/eV is calculated by

$$D(E) = \frac{T}{2\pi N} \sum_{\pm} \sum_{\mu=1}^{N} \int \frac{1}{|\frac{dE_\mu^\pm(k)}{dk}|} \delta(E_\mu^\pm(k) - E) dE \tag{3.19}$$

where the summation is taken for the N conduction $(+)$ and valence $(-)$ 1D bands. The 1D van Hove singularities (vHs) in the DOS, which are known to be proportional to $(E - E_0)^{-1/2}$ at the both the energy minimum and maximum $(\pm E_0)$ of the dispersion relations of SWNT, are very significant for determining solid state properties of SWNTs.

The DOS pictures for metallic and semiconducting SWNTs are derived [62] and qualitatively drawn in Fig. 3.8, together with their corresponding qualitative bandstructures. The energy differences $E_{11}^M(d_t)$ and $E_{11}^S(d_t)$ for metallic and semiconducting SWNTs between the highest π^* valence band singularity and the lowest π conduction band singularity in the 1D DOS curves are derived based on Eq. (3.18),

respectively, as:

$$E_{11}^{M}(d_t) = 6a\gamma_0/d_t, E_{11}^{S}(d_t) = 2a\gamma_0/d_t \tag{3.20}$$

3.2 Optical Properties

3.2.1 Single-Walled Carbon Nanotubes

The optical properties of SWNTs, i.e., how light interacts with SWNTs, are largely dependent on their electronic energy bandstructures introduced in the last subsection. As Fig. 3.8 shows, possible optical transitions Epp' from the p-th valence band to the p' conduction band occur following the selection rules of $\delta p = 0$ and $\delta p = \pm 1$ for parallel and perpendicular polarizations of the electric field component of light with respect to the nanotube axis, respectively [63]. However, for the perpendicular polarization case, the optical transition is greatly suppressed by the depolarization effect [63]. Thus, we only consider the optical absorptions for the parallel polarization case, i.e., $\delta p = 0$, which are noted in Fig. 3.8 by E_{11}^{M}, E_{11}^{S}, E_{22}^{S}, and E_{33}^{S}.

So far, experimentally, most of the SWNTs samples people use are metallic-semiconducting mixed and ranging of various tube diameters. Pioneering work on SWNTs' optical absorptions was performed by Kautaura *et al.* as shown in Fig. 3.9, where they used four different types of SWNTs samples of four different average diamters prepared by both laser vaporization and DC arc discharge, with catalysts of NiY (4.2 − 1 at .%), NiCo (1.2 at .%), Ni (0.6 at .%) and RhPd (1.2 at .%), respectively [64].

As the optical absorption spectra show, besides the 0.55 eV and 0.9 eV small absorption peaks due to the quartz substrates, three large and similar absorption peaks arising from SWNTs themselves are observed for all these samples, with varying

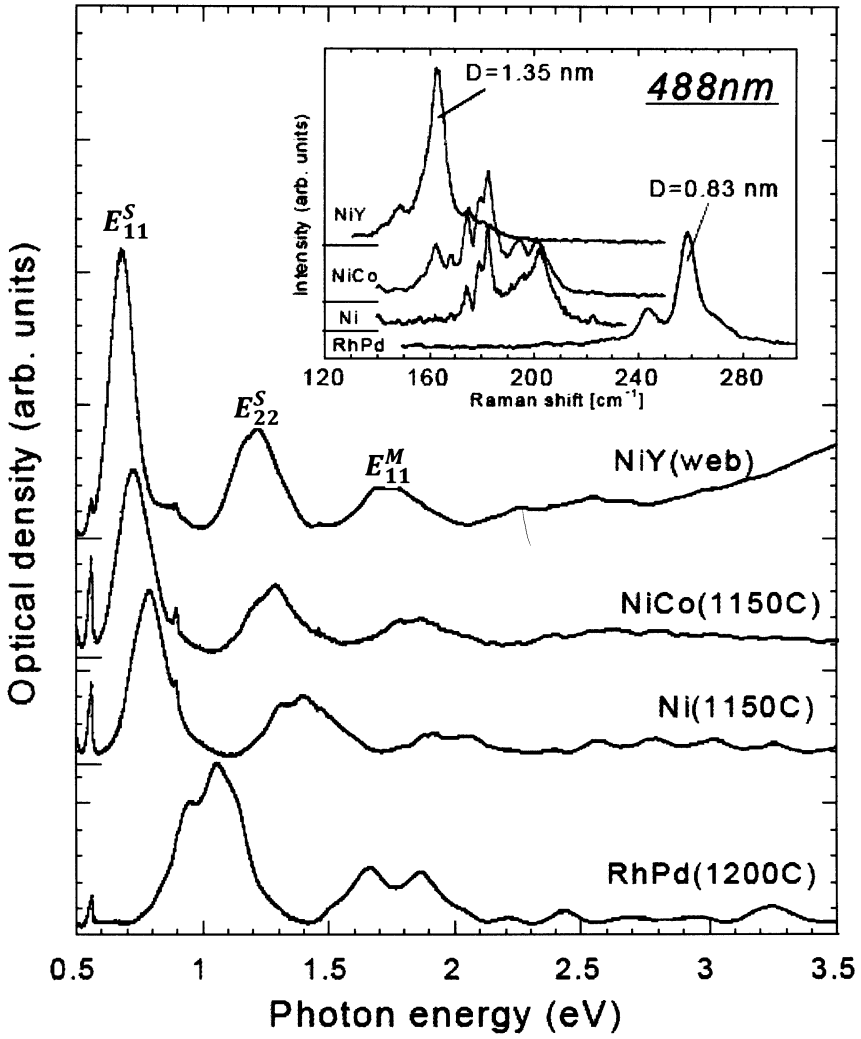

Figure 3.9 : Optical absorption spectra for four types of SWNTs with different diameter distributions. The inset shows their corresponding RBM modes of Raman spectroscopy obtained at 488 nm laser excitation, which estimate the diameter distribution. Adapted from [64].

peak positions because of the different nanotube diameters. 1D band calculation and resonance Raman scattering indicate that the first and second lowest peaks come from the optical absorptions corresponding to E_{11}^S and E_{22}^S, and the third is due to E_{11}^M. Diameter distributions can also be estimated from this absorption spectrum, just like the radial breathing mode in Raman spectra, by the peak position since it is dependent on the tube diameter, as indicated by Eq. (3.20). Moreover, the mixture ratio between the metallic and semiconducting SWNTs can also be roughly obtained by the ratio of their corresponding absorption peak intensities [64].

Although each SWNT has its own special 1D bandstructure and DOS for its assigned chirality (n, m), usually SWNTs in ensemble samples are bundled with each other and they lose their intrinsic 1D electronic state properties. For example, the absorption peaks for bundled SWNTs samples in Fig. 3.9 are broad due to tube aggregation and actually contain a number of individual peaks for individual SWNTs. Recently, people have made significant progress on the individualization of SWNTs. For example, in the pioneering work by the Smalley group here at Rice in 2002, individual SWNTs were obtained with each encased in a cylindrical micelle, through an ultrasonical agitation of an aqueous dispersion of raw SWNTs in sodium dodecyl sulfate (SDS) and then a following centrifugation to remove tube bundles, ropes, and residual catalyst [65]. The optical absorption spectra of such individualized SWNTs prepared via a similar way are shown in Fig. 3.10(a) [66], from which we can see obvious individual optical absorption peaks within E_{11}^S and E_{22}^S regimes, each assigned to specific chirality indices (n, m).

Furthermore, recently, great progress made on metallic-semiconducting SWNT separation has opened up new possibilities for nanotube-based nano-device applications. Among all kinds of those separation methods, density gradient ultracentrifu-

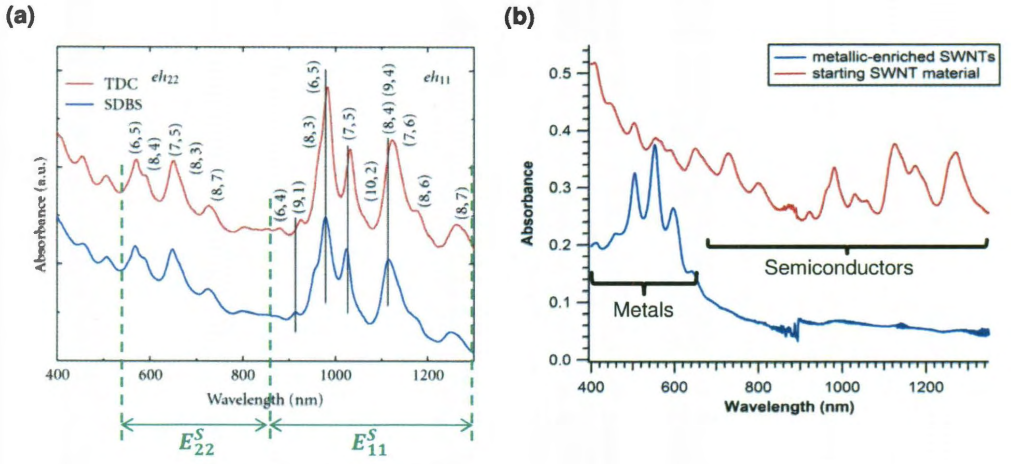

Figure 3.10 : (a) Optical absorption spectrum of individualized CoMoCAT SWNTs dispersed in DI water using TDC (red line) and SDBS (blue line) as surfactant. The absorption peaks from different SWNT species are assigned with their chirality indices (n, m). Adapted from [66] (b) Optical absorption spectra of metallic enriched HiPco SWNTs separated out through DGU (blue line) and their starting as-produced mixed HiPco SWNTs (red line). Reproduced from [67]

gation (DGU) is an excellent one developed by the Hersam group at Northwestern University [68]. Here at Rice, my groupmate Erik Hároz has made significant improvements on SWNT DGU separation. As an example, a nice optical absorption spectrum is shown in Fig. 3.10(b), in which both the metallic-semiconducting separation and SWNT individualization are fulfilled [67].

For a semiconducting SWNT, the physical process following optical absorption is fluorescence emission, or photoluminescence (PL). As the qualitative 1D DOS diagram shown in Fig. 3.11 (a), optical absorption at photon energy E_{22} is followed by fluorescence emission near E_{11}. The values of E_{11} and E_{22} vary with SWNT structure. Solid arrows indicate radiative excitation and emission transitions, while the dashed arrows indicate nonradiative relaxation of the electron (in the conduction band) and hole (in the valence band) before emission. Obviously, this PL process only happens

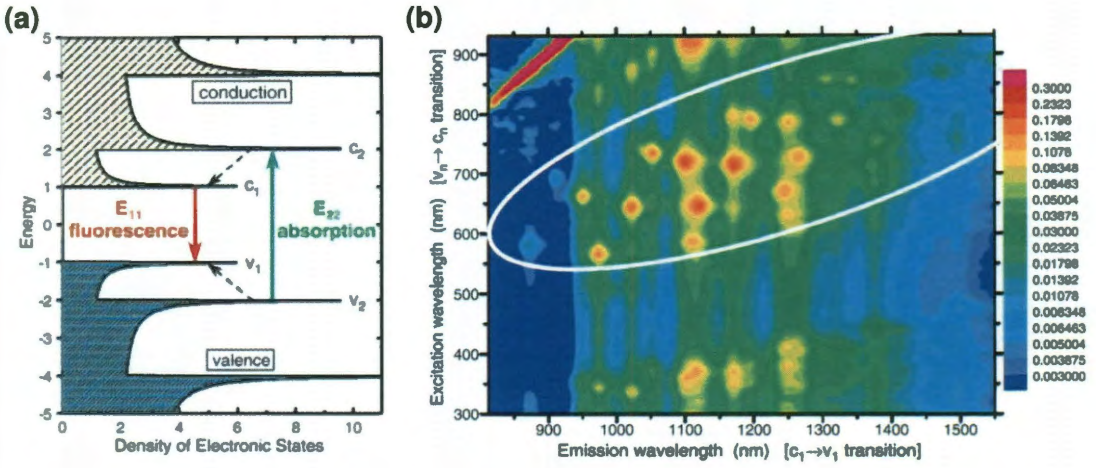

Figure 3.11 : (a) 1D density of states diagram of a semiconducting SWNT showing the photoluminescence process. (b) PLE map of a HiPco-grown SWNTs sample suspended in SDS and deuterium oxide. Reproduced from [69]

in semiconducting SWNTs, and metallic ones do not show PL since they have finite DOS at the Fermi level.

The Weisman group here at Rice systematically studied fluorescence emission from individualized HiPco (high-pressure carbon monoxide) grown SWNTs suspended by SDS surfactant in deuterium oxide [65] as a function of both excitation wavelength (from 300 nm to 930 nm) and emission wavelength (from 810 nm to 1550 nm), and the results are demonstrated in Fig. 3.11(b) as a contour plot [69]. This type of contour map is called a PL excitation (PLE) map. The white oval in the figure circles a region of discrete peaks arising from the transitions shown in Fig. 3.11(a), which correspond to various (n, m) semiconducting SWNT species [69, 70]. This type of spectroscopy is useful to determine the chirality indices (n, m) of the semiconducting SWNTs in an ensemble sample.

Both the optical absorption and photoluminescence processes discussed above are

strongly affected by excitons, or correlated electron-hole pairs [71]. The presence of excitons with a significant binding energy creates new electronic states between the lowest vHs conduction band and the highest vHs valence band for semiconducting SWNTs, which leads to novel optical properties different from the optical transitions described by a simple band picture shown in Fig. 3.11(a). Exciton effects are stronger in SWNTs than in conventional semiconductor such as GaAs due to the specially strong 1D electron-hole Coulomb interactions. A two-photon PLE study done by Wang *et al.* [72] exhibited exciton binding energy of $\sim$ 400 meV for 0.8 nm diamter semiconducting SWNTs.

Excitons modify optical absorption peaks by strongly changing their profiles and intensities. More importantly, special internal structure of excitons in SWNTs can be one reason for the low photoluminescence quantum yields of SWNTs, $\sim 10^{-3}$ to 10^{-4}. Such a tiny portion of absorbed photons are re-emitted in fluorescence while the majority seem to decay non-radiatively [65, 73]. This is an outstanding problem for SWNTs optics. Below the first optically active exciton state, there are also optically inactive dark excitons, which can trap much of the exciton population at low temperature. Our research group at Rice has recently made great progress on the observation of those dark excitons [22], and brightening them through a magnetic field and then increasing the photoluminescence quantum yield of SWNTs drastically by as much as a factor of 6 at low temperatures [74].

3.2.2 Graphene

The unique optical properties of graphene also arise from its exceptional electronic energy band structure. Figure 3.12 shows a Dirac cone near the $\boldsymbol{K}$ or $\boldsymbol{K'}$ point (Dirac point, as we discussed in §3.1.1). As-grown graphene samples in air are usually p-

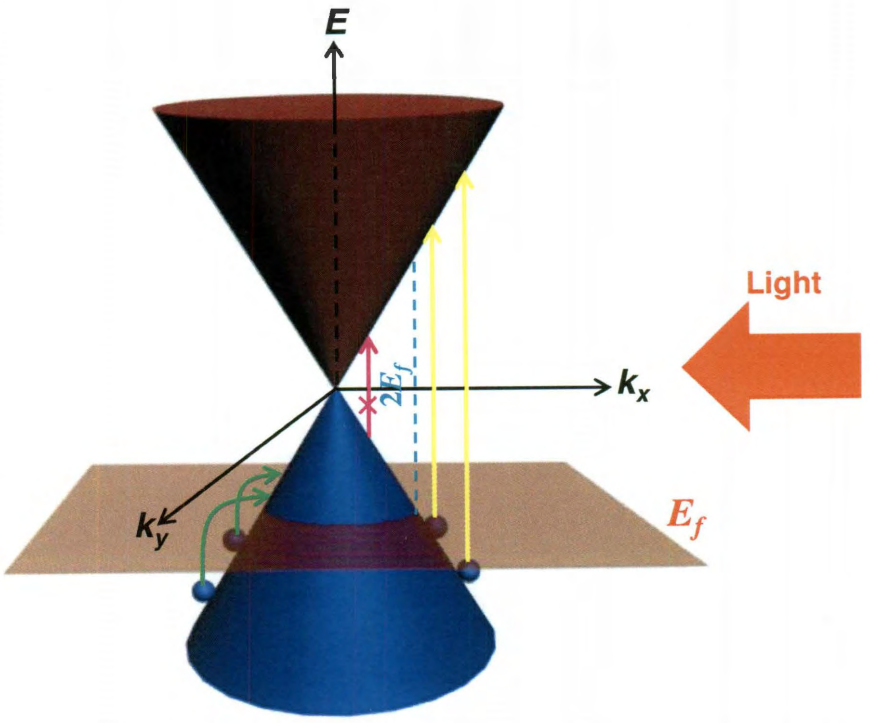

Figure 3.12 : Electronic energy bandstructure of a typical p-doped graphene, illustrating the two types of optical behavior: intraband absorption (green arrows) and interband absorption (yellow arrows).

doped already, as explained in Chapter 7, so the Fermi level (E_f) is drawn inside the π^* valence band.

As light illuminates graphene, two different photon absorption processes occur. When the photon energy is as small as several meV, electrons in the valence band can absorb that energy and move to higher states (green arrows) within the valence band. This process, intraband dynamics, could be described by the Drude model. When the photon energy is smaller than $2E_f$, no interband transition would happen because of the Pauli blocking (pink arrow). However, when the photon energy reaches

$2E_f$, electrons in the valence band below the Fermi level start absorbing light to jump into the conduction band vertically (yellow arrows), which results in the so-called interband conductivity.

The photon energy ranges where these two processes occur depend on the carrier mobility and concentration of the graphene sample. For a typical graphene sample grown by chemical vapor deposition (CVD), usually the intraband absorption takes place in the THz and mid-infrared ranges, while the interband absorption occurs in visible and near infrared (NIR) ranges. We will discuss the interband optical absorption in this subsection, and discuss the intraband conductivity in the next section in terms of THz spectroscopy of graphene.

Theoretical studies suggest that the interband absorption for a single-layer graphene should be a constant, $\pi\alpha \approx 2.3\%$, which is called the universal optical absorption, and the corresponding dynamic conductivity is called the universal optical conductivity [75]. Here α is the fine structure constant (=1/137). The first observation of such universal optical absorption for graphene was made by Geim's group at the University of Manchester in 2008 [44], in which a wavelength independent opacity of 2.3 $\pm$ 0.1% and negligible reflectance (<0.1%) were measured (Fig. 3.13 (B)). That constant opacity was also found to increase with the number of layers of the graphene sheets so that each one adds another 2.3% (Fig. 3.13 (B) inset). An actual photograph of their graphene samples in transmitted white light at a 50-μm aperture is shown in Fig. 3.13 (A). The suspended graphene was partially covered in the aperture so that opacities of different areas can be compared. The yellow line scan across the image qualitatively illustrates changes in the observed light intensity.

In graphene, at the $2E_f$ onset, the universal optical absorption starts from zero, as we discussed above. Basov's group at the University of California at San Diego

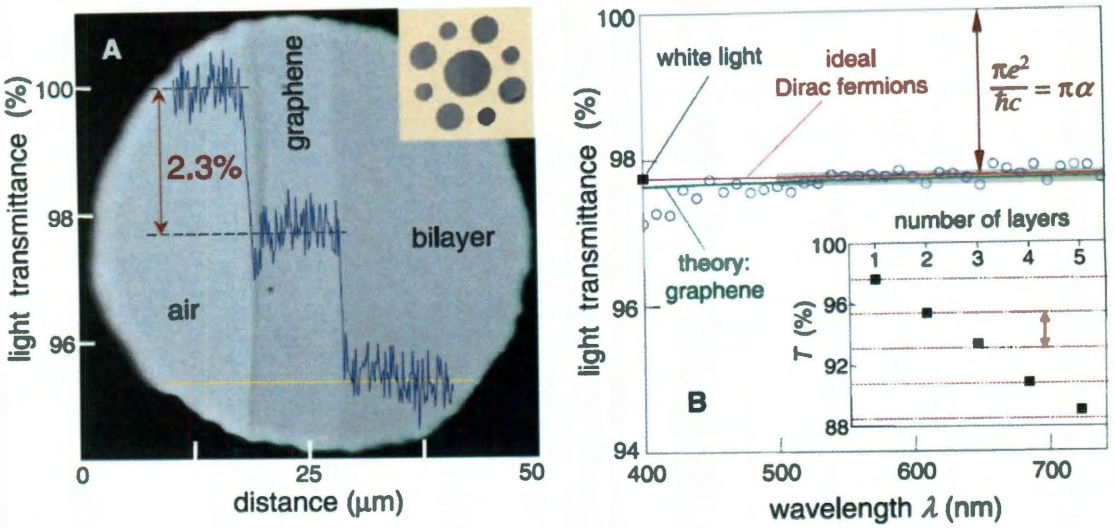

Figure 3.13 : (A) Photograph of a 50-μm aperture with the suspended graphene partially covered, different optical opacities at different regimes are illustrated. (B) Optical transmittance of the single-layer graphene in visible range, inset shows the transmittance of the while light as a function of number of graphene layers. Reproduced from ref. [44]

has conducted gate-voltage-dependent infrared spectromicroscopy measurements on a monolayer graphene sample [76]. As Fig. 3.14 shows, as the gate voltage was varied, the $2E_f$ onset for the universal optical conductivity $\pi e^2/2h$ clearly shifted to higher photon energies.

3.3 Terahertz Dynamics

3.3.1 Single-Walled Carbon Nanotubes

The optical properties we described in subsection §3.2.1 are mostly focused on semiconducting SWNTs, whose main features occur in the visible/NIR range. In this subsection, we focus on the lower energy range, i.e., THz frequency range, which should be the right stage for metallic SWNTs instead. The THz dynamics of 1D

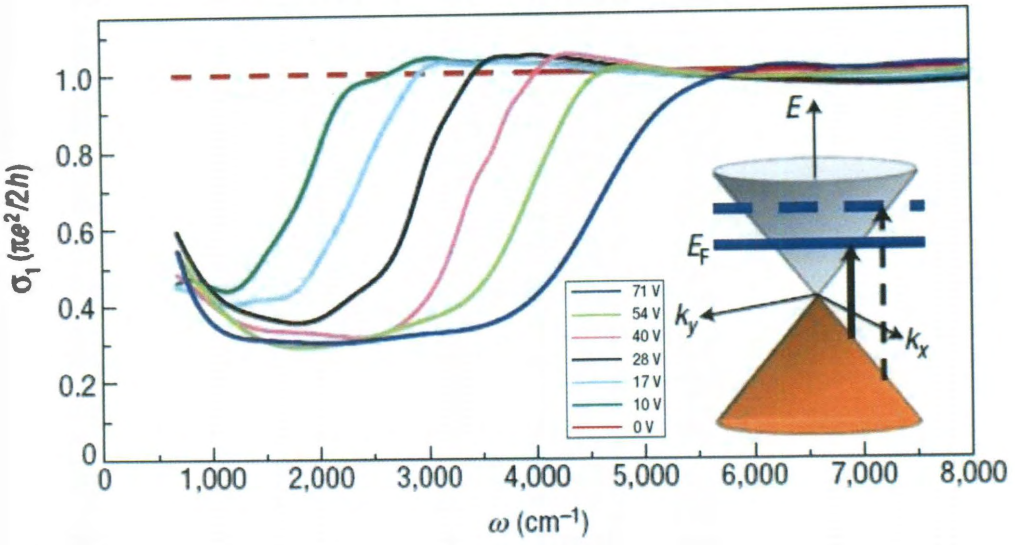

Figure 3.14 : Optical conductivity (proportional to optical absorption) spectrum in infrared range for mechanically cleaved graphene sample under different gate voltages. Reproduced from ref. [76]

interacting electrons are expected to be highly unusual from a fundamental point of view.

Over the past decade, a variety of THz/FIR spectroscopic research has been experimentally performed on various forms of SWNTs [77–86]. As a result, there are now conflicting results as well as contradicting interpretations. This can be explained in part by the wide range of sample types used in these studies resulting from different growing methods (HiPco, CoMoCAT, CVD, and laser ablation) and placement in a variety of polymer films transparent in the THz range. Most samples consisted of bundles of both semiconducting and metallic nanotubes with a wide distribution of diameters. Other samples were partly aligned by mechanical stretching, resulting in an anisotropic THz response [80, 81, 83]. One similarity across these experiments is the observation of non-Drude-like THz frequency dependence and the detection of

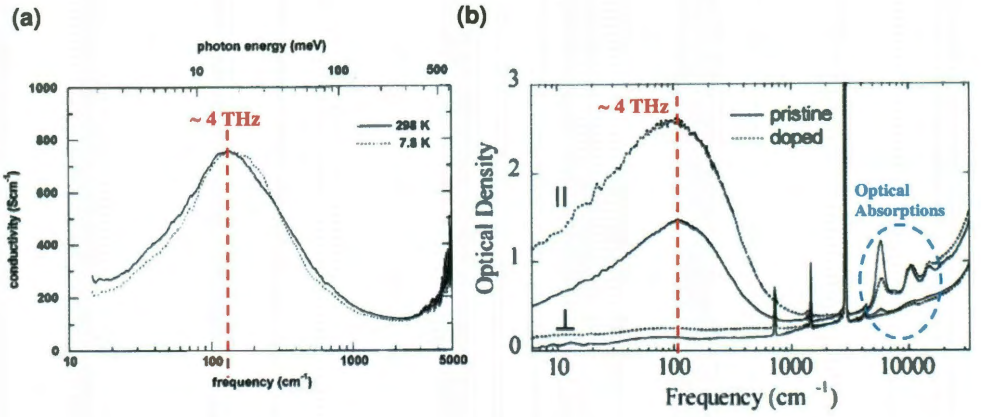

Figure 3.15 : (a) Real part of dynamic conductivity of laser-vaporization-grown SWNTs sample extracted from the IR reflectance spectrum, exhibiting a broad $\sim$ 4 THz absorption peak robust to temperature change. Adapted from Ref. [78]. (b) Polarized absorption spectra of pristine (black lines) and tetrafluorotetracyanoquinodimethane (F_4TCNQ)-doped (dashed lines) L-SWNTs films. The $\sim$ 4 THz absorption peak is dramatically enhanced in doped L-SWNTs without notable change in the peak position, while the optical absorption peaks are greatly suppressed there. Adapted from Ref. [83]

an absorption peak around 135 cm^{-1} (or $\sim$ 4 THz or $\sim$ 17 meV). First observed by Ugawa *et al.* [78] in the real part of the conductivity (Fig. 3.15 (a)), this feature has been interpreted as either interband absorption in metallic (or mod 3) nanotubes with curvature-induced gaps [78, 85, 86] or absorption due to classical plasmon oscillations along the tube axis [83]. Currently, a consensus has not been achieved.

As Fig. 3.15 (a) shows, Ugawa *et al.* measured the IR reflectance spectrum of a free standing laser-vaporization-grown SWNTs film over $15 - 5000$ cm^{-1} ($2 - 620$ meV, $0.45 - 150$ THz), and extracted out the real part of the THz/IR dynamic conductivity by Kramers Kronig transformation. We can see there is a broad absorption peak around $\sim$ 135 cm^{-1} ($\sim$ 4 THz), the origin of which is currently under hot debate as we stated above. During the experiment the SWNTs sample was located in a liquid

helium flow cryostat, so temperature dependent measurements were also performed. However, as we see in Fig. 3.15 (a), that absorption peak was quite robust and not affected by the huge temperature change.

Akima *et al.* obtained the transmission spectra for doped and undoped laser-ablation-grown SWNTs (L-SWNTs) embedded in polyethylene matrices in a wider range ($6 - 33000$ cm^{-1}). Mechanical stretch also made the nanotubes in the polymer matrices aligned to some degree and anisotropic response of such samples were studied, as shown in Fig. 3.15 (b). As we can clearly see, when the light polarization was parallel with the nanotube axis, a similar broad $\sim$ 4 THz absorption peak was observed. Since the spectrum range is very wide and extended even to the visible range, those optical absorption peaks arising from interband transitions (illustrated in Fig. 3.8) were also revealed (in the turquoise dashed oval). Compared with the parallel case, the absorptions were greatly suppressed for the perpendicular case in the THz/FIR range, which suggests a 1D THz dynamics for the carriers in SWNTs. However, they were not zero after all, the possible reason is the degree of nanotube alignment in their samples was not high enough. Doping significantly increased the intensity of that THz/FIR absorption peak, while it drastically decreased the intensities of optical absorptions peaks, which further indicate the THz/FIR dynamics of SWNTs is intraband behavior, essentially different from the interband transitions in the UV/visible/NIR range.

3.3.2 Graphene

As we discussed in §3.2.2, for graphene, an intraband conductivity would dominate the THz/FIR range, which was also predicted by previous theoretical studies [87, 88]. Its first experimental demonstration was performed by Kaindl's group at the

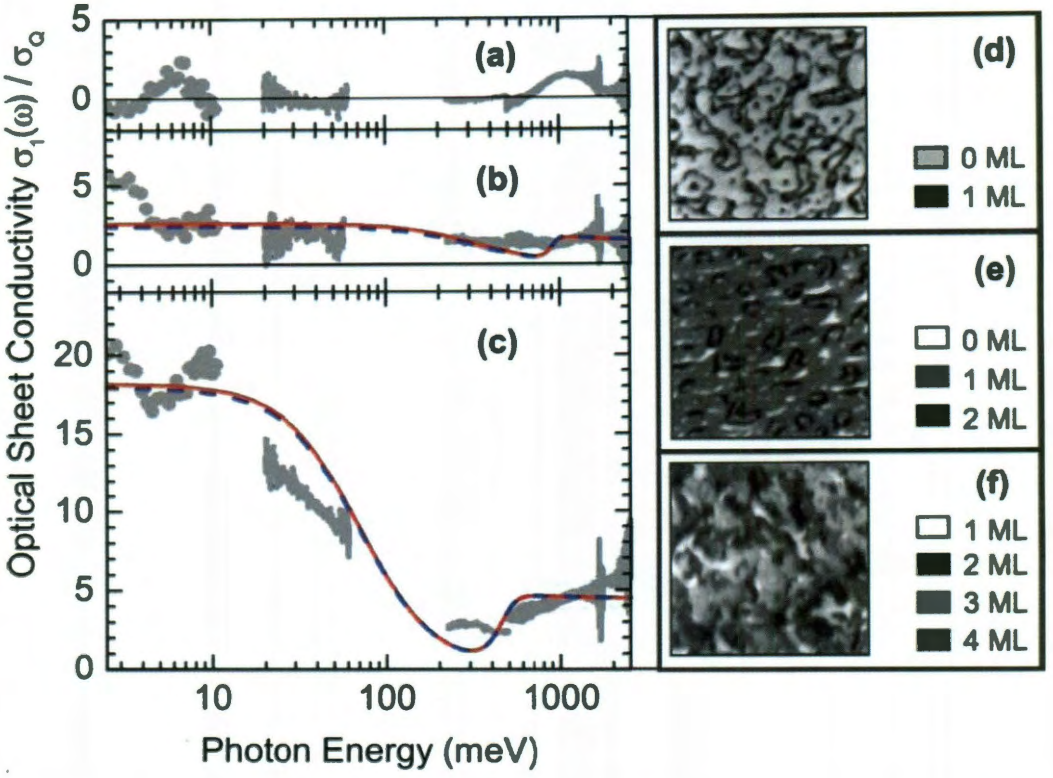

Figure 3.16 : Real part of the optical sheet conductivity (gray), normalized by the universal optical conductivity value $\sigma_Q = \pi e^2/2h$: (a) buffer layer, (b) monolayer graphene, (c) multilayer graphene; (d) – (f) $2.5 \times 2.5\ \mu m^2$ LEEM images of nominally buffer, monolayer, and multilayer graphene. Reproduced from Ref. [89]

Lawrence Berkeley National Laboratory [89]. They measured the transmission spectra of epitaxial graphene samples grown via thermal decomposition by combing THz time-domain spectroscopy and Fourier transform infrared spectroscopy (FTIR), and real parts of dynamic conductivities were calculated and plotted in Fig. 3.16. Compared with the insulating response from the reference buffer, both the mono- and multilayer graphene samples exhibited Drude-like THz/FIR intraband conductivities, together with their interband absorptions in the optical range.

Horng *et al.* performed gate-voltage-dependent FTIR measurements on CVD grown graphene, and obtained Drude-like intraband THz/FIR conductivities at different carrier concentrations followed by corresponding Drude-model fittings to extract out the carrier scattering rate Γ and Drude weight $D = \frac{v_F e^2}{\hbar}\sqrt{\pi|n|}$ (n is the carrier concentration) [46]. Their results are shown in Fig. 3.17. From Fig. 3.17 (a) and (b) we can see that the real parts of gate-induced AC conductivity change $\Delta\sigma'$ can be fit well by the Drude model, but the obtained Drude weight D was not symmetric between the hole side and electron side, as shown in (d). For the same induced gate voltage, the Drude weight (or free carrier concentration) on the electron side is smaller, which was explained as the role played by electron-impurity interactions. Also, notablely, the experimentally determined D values (black square) were lower than the theoretical predictions (blue dashed line) by $20 - 45$ %, which indicated an appreciable electron-electron interactions due to pseudo-spin physics.

Furthermore, Ju *et al.* in the same group converted the CVD grown graphene film used in [46] into aligned graphene micro-ribbon arrays in a 2.5×2.5 mm^2 area at the center through standard optical lithography followed by oxygen plasma etching [17]. Polarization dependent FTIR transmission measurements were performed, the results of which are shown in Fig. 3.18. When the polarization was parallel to the graphene micro-ribbon alignment, the gate-induced transmission change exhibited Drude-like frequency dependence, indicating a free carrier oscillation, as (a) shows. For the perpendicular case in (b), however, a prominent absorption peak at ~ 3 THz (~ 100 cm^{-1}) appeared because of the plasmon excitation arising from the collective oscillations of electrons across the width of micro-ribbons. Their further measurements demonstrated that plasmon resonance could be quantitatively tuned by adjusting the induced gate voltage and ribbon width. This strong and tunable plasmon-light cou-

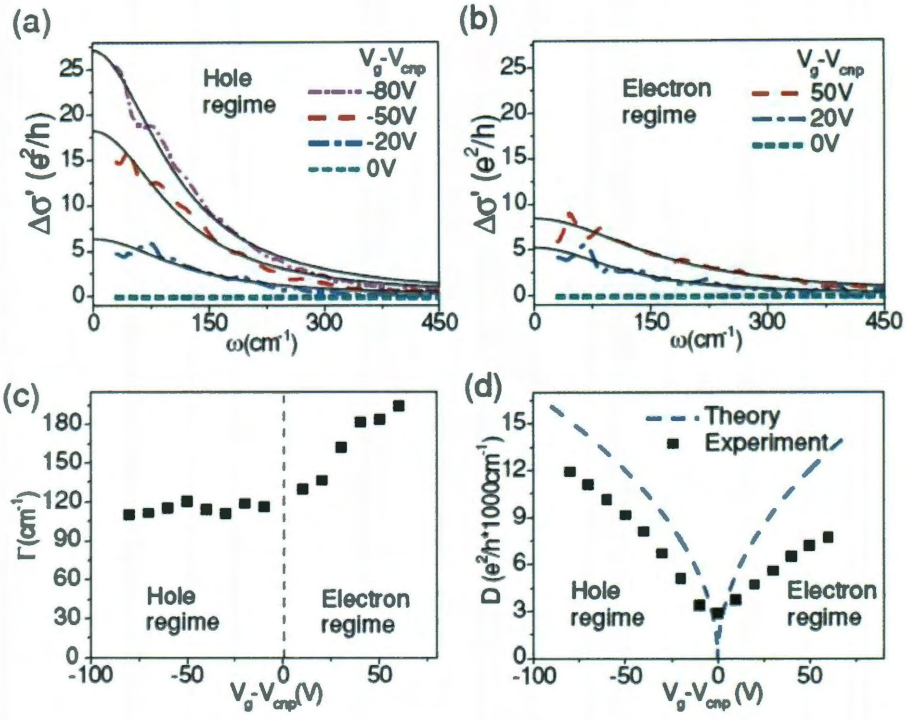

Figure 3.17 : (a) and (b) Gate-voltage-induced AC conductivity change $\Delta\sigma'$ together with its Drude-model fitting in hole- and electron- doped graphene, respectively, in the range 30 – 450 cm^{-1} (0.9 – 13.5 THz). (c) and (d) The scattering rate Γ and Drude weight D fit for different hole and electron concentrations. Reproduced from Ref. [46]

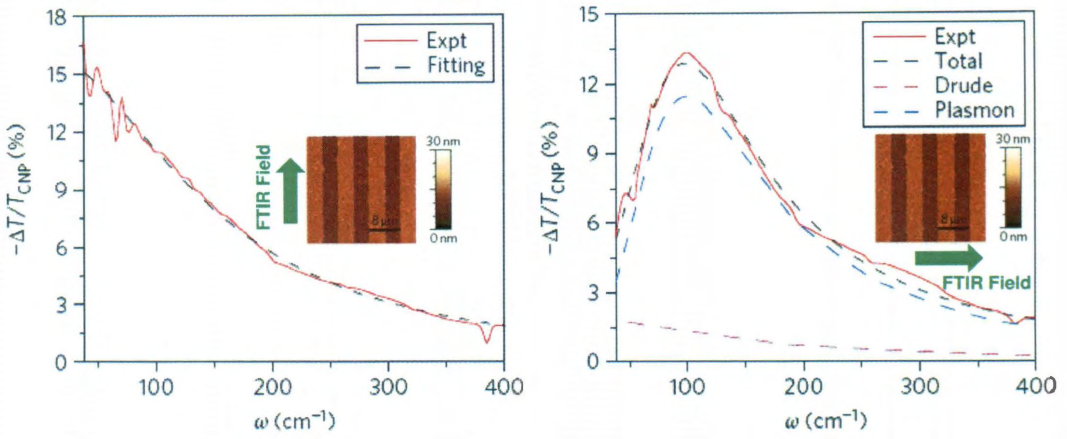

Figure 3.18 : Gate-induced change of transmission spectra (red solid line) of aligned graphene micro-ribbon arrays, with the ribbon alignment parallel (a) and perpendicular (b) to the incident light polarization, together with the free carrier fitting by Drude model and plasmon resonance fitting by a Lorentzian lineshape. Inset shows an AFM image of a graphene micro-ribbon array sample with ribbon width of 4 μm and a ribbon-gap width ratio of 1:1. Adapted from Ref. [17]

pling, together with its own excellent optelectronic properties we discussed in Chapter 1 and its remarkable compatibility with micro-/nano- fabrication, provides graphene a promising potential for THz metamaterials and optoelectronic devices.

Currently, there are many theoretical studies predicting novel phenomena for graphene-based THz dynamics and optoelectronic applications due to its unique linear dispersion bands tructure combined with many-body interactions. In contrast, however, publications on experimental work have been limited. Now I will introduce two important theoretical predictions on graphene AC dynamics.

The first is the work by Mikhailov *et al.*, in which the linear bands of graphene are expected to lead to highly nonlinear dynamics [90]. As an example, let us discuss some differences between electrons in the conventional semiconductor GaAs and graphene in their responses to an applied AC electric field $E_x(t) = E_0 \cos\omega t$. After solving the

classical equation of motion, we find that the resulting current in the case of GaAs with a parabolic dispersion $\varepsilon(\boldsymbol{p}) = |\boldsymbol{p}|^2/2m^*$ (m^* is the electron effective mass) is given by the following expression, which oscillates at the same frequency ω as the applied AC electric field:

$$j_x(t) = \frac{n_s e^2 E_0}{m^* \omega} \sin \omega t. \tag{3.21}$$

On the other hand, in the case of Dirac fermions in graphene with a linear dispersion $\varepsilon(\boldsymbol{p}) = V|\boldsymbol{p}|$ (V is the Fermi velocity), the resulting current has a very different expression.

$$j_x(t) = e n_s V \frac{4}{\pi}(\sin \omega t + \frac{1}{3} \sin 3\omega t + \frac{1}{5} \sin 5\omega t + \cdots). \tag{3.22}$$

As we can see, not only does the resulting current oscillate at the frequency of the applied field ω, but it also contains all the odd-harmonics 3ω, 5ω, 7ω, ... Therefore, the dynamics of graphene in an AC electric field are intrinsically nonlinear, and frequency multiplications are expected for future THz device applications, since the experimental parameters (for example, relevant density $n_s \sim 10^{11}$ cm^{-2}, ...) predict this to happen significantly in the THz and sub-THz range.

The other fascinating theoretical prediction is THz radiation generation from optically pumped graphene by Ryzhii *et al.* [38]. As Fig. 3.19 shows, based on their developed model, they calculated the dynamic conductivity of a nonequilibrium 2D electron-hole system in graphene under interband optical excitation. Both interband and intraband transitions are taken into account in this model. Under the optical pumping with photon energy $\hbar\Omega$, electrons and holes are photogenerated with energy $\varepsilon_0 = \hbar\Omega/2$ and emit a cascade of optical phonons with energy $\hbar\omega_0$, and then populate the lower and lower states by a step of $\hbar\omega_0$, which might lead to a population accumulation of the bottom of conduction band (by electrons) and the top of valence band (by holes). They demonstrated that sufficiently strong optical pumping may result in

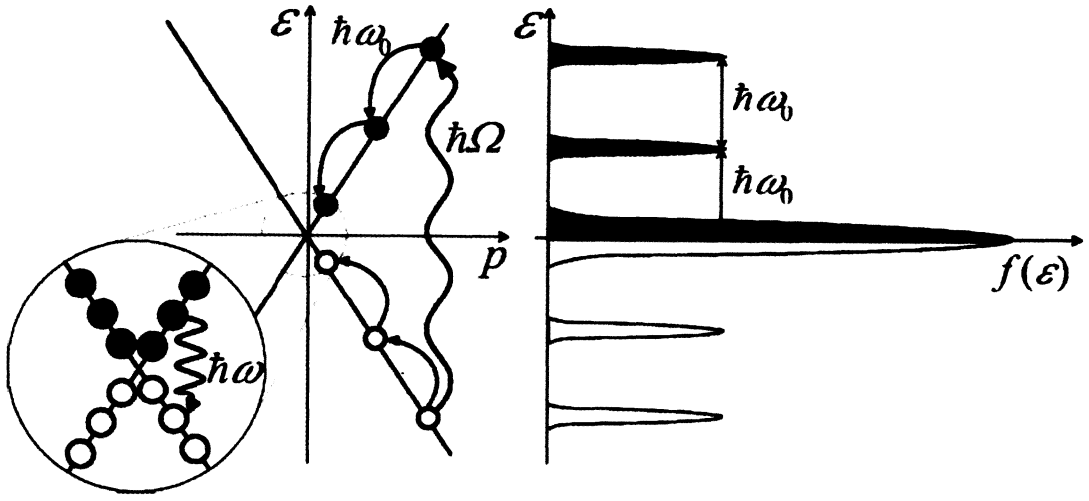

Figure 3.19 : Sketch of graphene bandstructure and energy distributions of photo-generated electrons and holes under interband optical pumping of photon energy $\hbar\Omega$. A cascade of phonons emission ($\hbar\omega_0$) is expected, so is the photon radiation ($\hbar\omega$) for sufficiently strong optical pumping. Reproduced from Ref. [38]

the population inversion in graphene, so that the real part of the net AC conductivity (proportional to absorption of radiation) can be negative, i.e., amplification. Due to the gapless energy spectrum, that negative AC conductivity takes place in the range of THz frequencies. This effect might be used in graphene-based coherent sources for THz radiation.

Chapter 4

Samples and Experimental Methods

4.1 Samples

As we discussed in the last chapter, two types of carbon nanomaterials were used for the terahertz (THz) conductivity work in this thesis: single-walled carbon nanotubes (SWNTs) and graphene.

4.1.1 Highly aligned SWNT films

Most of the SWNT samples used in previous THz studies described in §3.3.1contained randomly oriented carbon nanotubes with non-uniform lengths. Some others were partly aligned by mechanical stretching, resulting in an anisotropic THz response [80, 81, 83]; however, the degree of alignment for them was not that high and the tube lengths were not well defined, either. To better understand the intrinsic THz response of SWNTs, we need to have a bulk sample in which the nanotubes are highly aligned and have uniform lengths. Dr. Cary Pint and Dr. Robert Hauge in the Chemistry Department of Rice provided us with highly aligned SWNT samples, which opened up entirely new possibilities for THz conductivity measurements.

Unlike tedious top-down approaches required to generate precise material structures for aligned carbon nanotubes, the aligned SWNT films studied here were produced by natural self-assembly of SWNTs into densely-packed and highly-aligned macroscopic materials during SWNT synthesis. 2 μm wide pads of catalyst con-

taining 0.5 nm Fe and 10 nm Al_2O_3, having spacing of 50 μm between lines, were formed on a Si wafer by using optical lithography and electron-beam deposition. The catalyst pads were then grown in a hot-filament chemical vapor deposition (CVD) apparatus maintained at 750°C and 1.4 Torr utilizing a water-assisted growth process with C_2H_2 decomposition. The as-grown lines of aligned SWNTs initially adopt a vertical orientation with respect to the growth substrate with a length that can be determined based on the duration of catalyst exposure to the growth conditions. The as-grown highly aligned SWNTs in high aspect-ratio lines are shown in Fig. 4.1(a). Following the growth process, a high temperature (750°C) H_2/H_2O vapor etch was employed to free the catalyst-SWNT interface, allowing an efficient contact transfer of the vertically aligned SWNTs forest onto a sapphire substrate (Fig. 4.1(b) and Fig. 4.1(c)) after being cooled down to produce a horizontally highly aligned SWNTs film [91–96]. Fig. 4.1(d) and Fig. 4.1(e) show scanning electron microscope and optical microscope images, respectively, exhibiting the excellent SWNT alignment in the transferred structures.

This SWNT film transfer process utilized a technique that takes advantage of the strong van der Waals interaction between the SWNT in the structure and the host substrate, inspired by the gecko effect [97].

The benefit of this approach compared to other possible methods is the simplicity of the contact transfer process that makes this scalable to large areas. Although the specific growth system utilized in these experiments constrained our growth substrate size to $\sim 1 - 1.5$ cm^2, there are no known limitations in this approach that would inhibit scaling to full wafers or even continuous roll-to-roll growth and contact transfer techniques to yield high throughput production of THz devices [98].

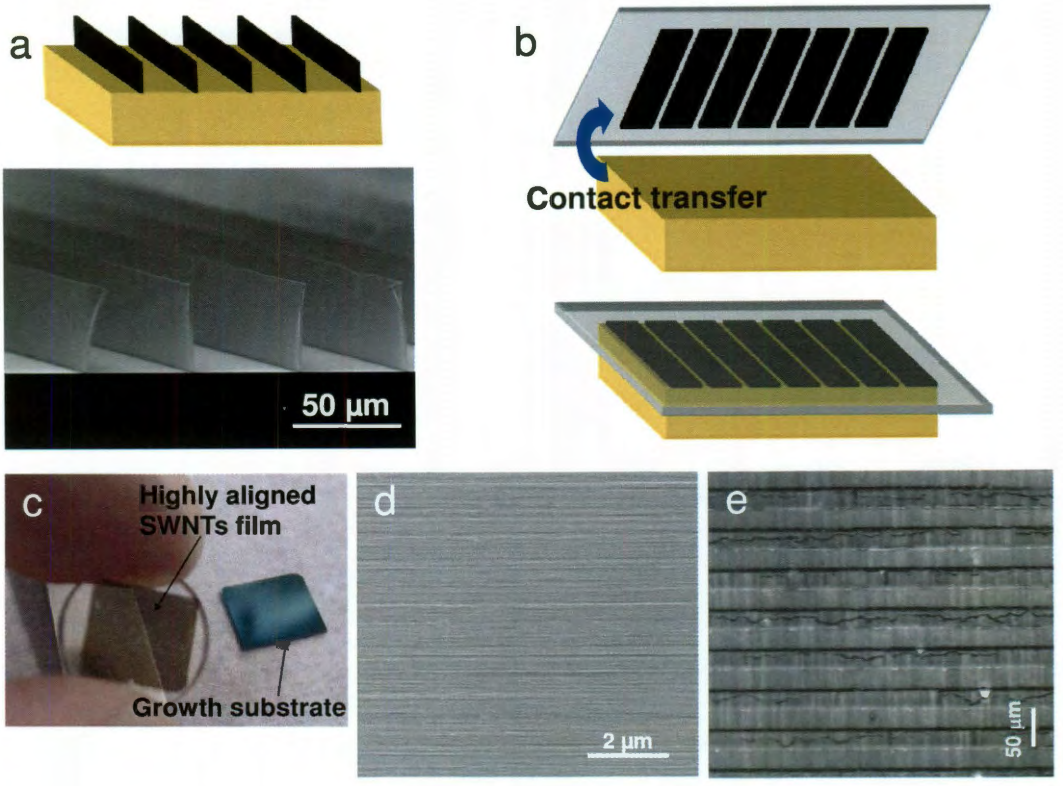

Figure 4.1 : Highly aligned SWNTs film: (a) Growth of upright SWNT lines using patterned catalyst substrates, (b) contact transfer of aligned SWNTs films to THz transparent sapphire substrates, (c) image showing as-transferred aligned SWNTs films and growth substrate from which transfer occurred, (d) – (e) scanning electron microscope and optical microscope images showing the excellent SWNTs alignment inside the transferred SWNT structures.

4.1.2 Large-area solid-state-grown graphene

The large-area graphene sample we used for this spectroscopy study was grown from a solid-state carbon source [99]. As Fig. 4.2 shows, a thin copper foil of centimeter scale was spin coated with a poly(methyl methacrylate) (PMMA) layer of the same size on it, and then was located into a typical tube furnace. At a temperature between 800°C and 1000°C, a reductive H_2/Ar gas flow was introduced under low pressure conditions. After about 10 minutes, a single uniform large-area layer of graphene was formed from the previous PMMA thin film, which was followed by another PMMA thin film spin coating on top of it in order to separate it. Afterwards a $CuCl_2$/HCl acid etch removed the initial Copper substrate and left the graphene/PMMA layer free to be transferred onto any substrate preferred for optical use. Here we chose THz/infrared(IR) transparent materials for the substrates, such as silicon. Finally, the top PMMA layer was soaked out in acetone, and the resulted graphene/substrate would be ready for THz/IR spectroscopy measurements. Due to the long characteristic wavelength of this interested optical frequency range, small-area graphene samples like exploited graphene or epitaxial graphene of only several microns won't work. Thus, "large-area" is one of the most important key points for the graphene sample to be studied on this purpose.

During the graphene growth process, by controlling the pressure of the reductive H_2/Ar gas, the number of graphene layers of the sample could be roughly controlled. Thus, we obtained single-layer, bi-layer, few-layer and many-layer graphene samples, and their characteristic Raman spectra are shown in Fig. 4.3(a). Raman spectroscopy confirms the number of layers for these samples through the G to G′ (2D) peak ratios as well as the exact peak positions & lineshapes of the G′ band. For single-layer graphene (red line), the G′ to G peak ratio is ~ 3, G′ peak sits at 2692.5 cm^{-1} and

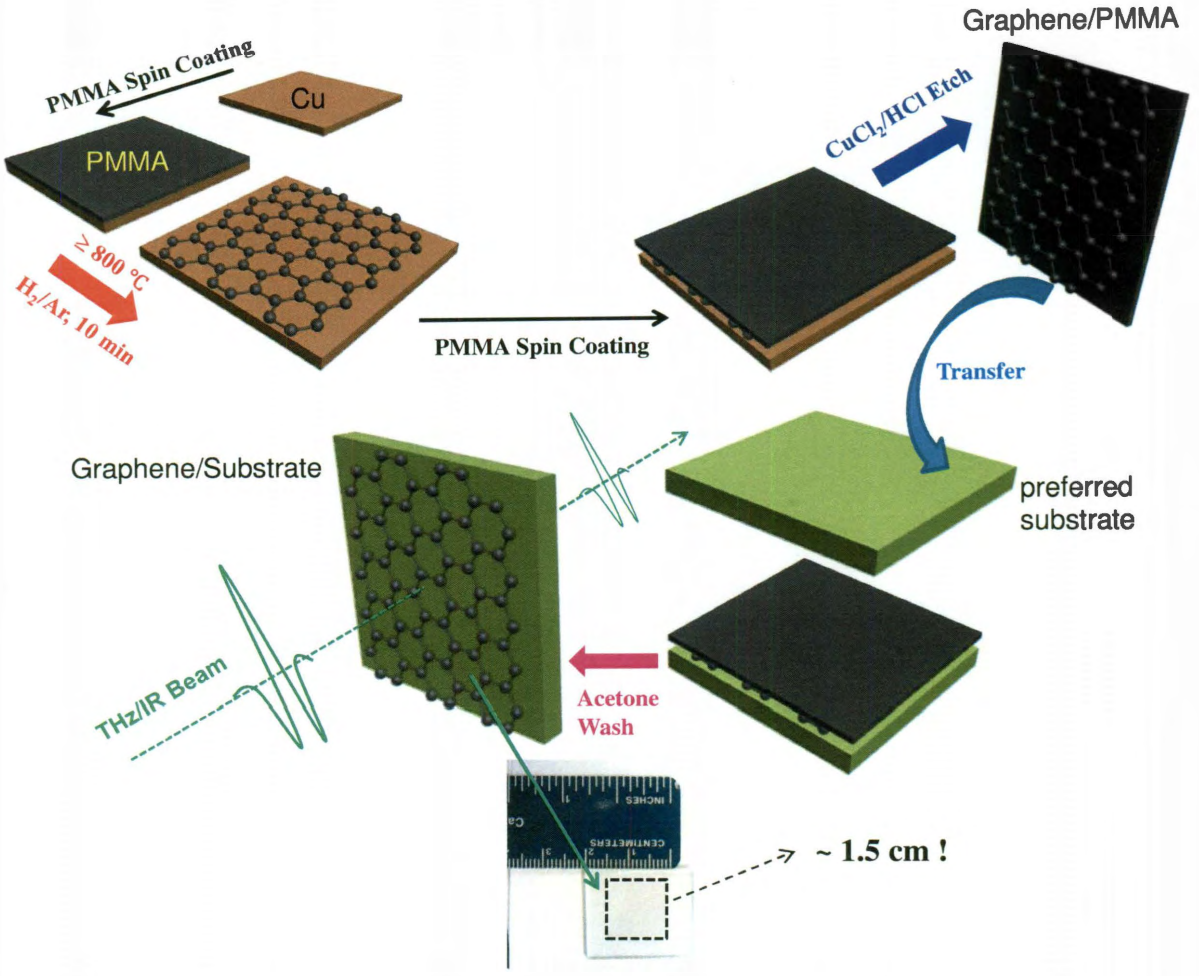

Figure 4.2 : Growth of large-area graphene from solid-state carbon source and its transfer for spectroscopy study.

has a symmetric Lorentzian shape with FWHM $\sim$ 30 cm^{-1}, which agrees with the knowledge from Ref. [100]. Figure 4.3(b) exhibits the ultraviolet (UV) – Visible – near infrared (NIR) transmittance lines, which showed flat spectral dependence with 2.3% per layer absorption, as demonstrated by many other groups [44, 76, 89]. In the UV part, they exhibit a characteristic 270 nm dip arising from the π-π^* transition. Three optical microscopy images of the single-layer, few-layer and many-layer graphene samples are shown in together with their optical transmittance lines correspondingly, in which we can see a good agreement between the trend of contrast ratios of the graphene-to-substrate and that of the optical transmittance values.

In order to study the intrinsic intraband and interband dynamics of graphene and its Fermi level, for its THz-TDS work in this thesis, we focus on the single-layer graphene samples.

4.2 THz-TDS system components

The THz time-domain spectroscopy (TDS) system utilized to measure the optical conductivity of SWNTs and graphene was described in §2.2 and illustrated in Fig. 2.1. Here in this section, we describe the components of this THz-TDS system and how they function.

4.2.1 Ti:Sapphire Laser

We used a mode-locked Ti:Sapphire laser (Coherent Inc., MIRA 900) pumped by a 5-W diode-pumped solid-state Nd:YVO_4 laser (Coherent Inc., Verdi). For the output Ti:Sapphire laser beam, the typical wavelength we used was $\sim$ 800 nm, and the repetition rate was $\sim$ 75 MHz, and the pulse width was $\sim$ 180 fs. The maximum average power we could obtain was $\sim$ 1 W for the continuous wave (CW) mode, and

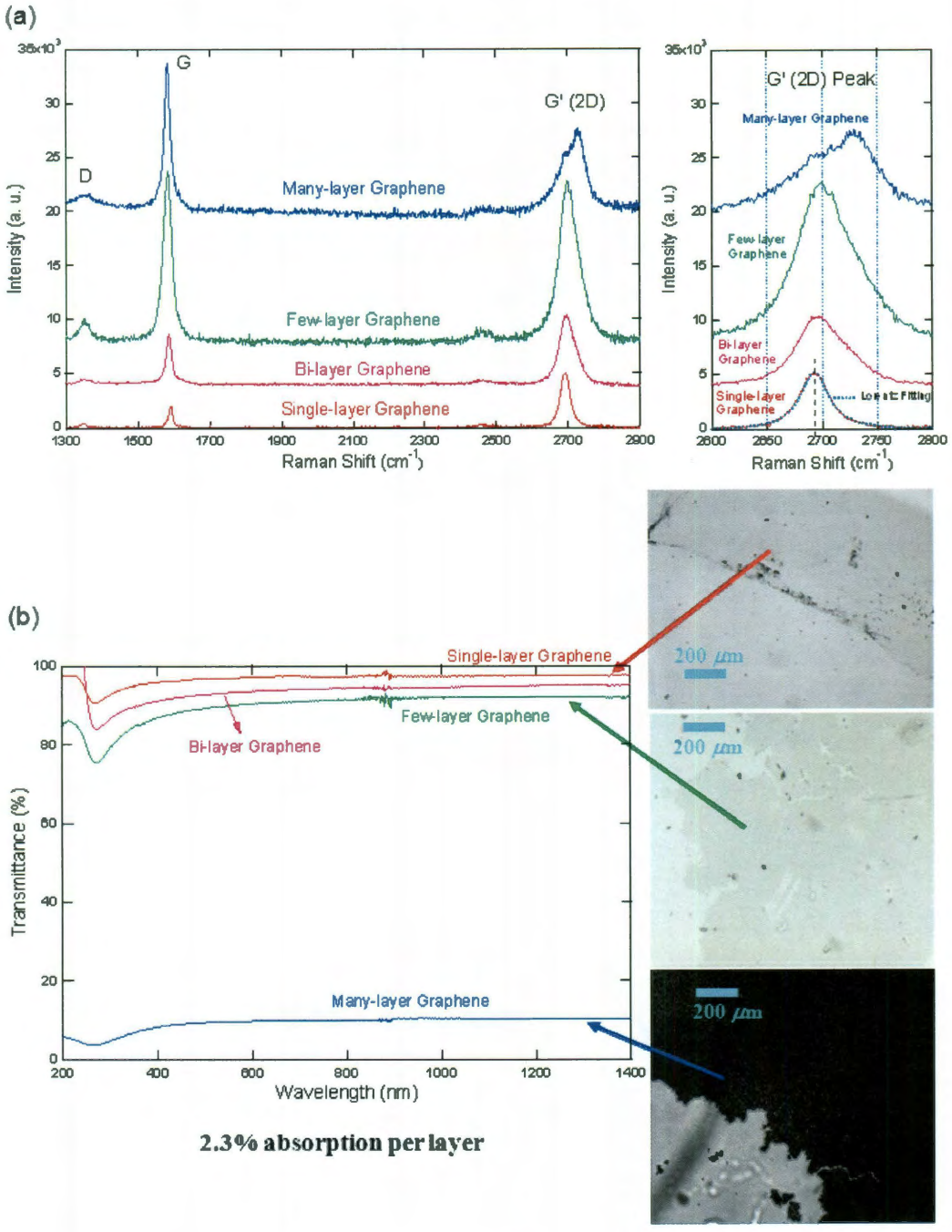

Figure 4.3 : (a) Raman spectrum and (b) UV-Visible-NIR transmittance spectrum together with optical microscopy image for single-layer (red), bi-layer (pink), few-layer (green) and many-layer (blue) graphene samples.

Figure 4.4 : Photograph of the Ti:Sapphire laser system. Left: Verdi solid-state green laser; Right: MIRA Ti:Sapphire laser.

$\sim$ 780 mW for the mode-locked (pulsed) mode at a good quality with fine output slit width. A cooling system (chiller) was utilized to keep both the laser diodes and Ti:Sapphire crystal at a proper working temperature $\sim$ 17 °C. Figure 4.4 shows the laser system (left: the Verdi solid-state green laser, right: the MIRA Ti:Sapphire laser).

4.2.2 Optical delay line

The optical delay is realized by an optical retro-reflector mounted on a motorized translation stage (UTM25PP.1, Newport Corp.), which could be computer-controlled by a motion controller (ESP 300, Newport Corp.), as Fig. 4.5 shows. There is another one-dimensional (1D) manual stage mounted between them to add more flexibility for time-delay adjustments. The retro-reflector provides a reflected optical beam in

Figure 4.5 : Photograph of the optical delay line. Top: motion controller; Bottom: retro-reflector and time-delay stage.

parallel with its incident beam. The motorized translation stage has a high resolution of 0.1 μm and moved at a step of 3.75 μm (corresponding to a time delay of 0.025 ps) per second for the THz signal scanning during the experiment.

4.2.3 THz emitter and detector

Our THz detector and first-version THz emitter are photoconductive antennas built on low-temperature-grown GaAs substrates, described in §2.2.1 and §2.2.2 in detail. Both of them were fabricated in clean rooms by photolithography, and provided to us by Prof. Tonouchi's group at Osaka University and Prof. Mittleman's group here at Rice separately. Figure 4.6 shows an optical microscopy image of the dipole of

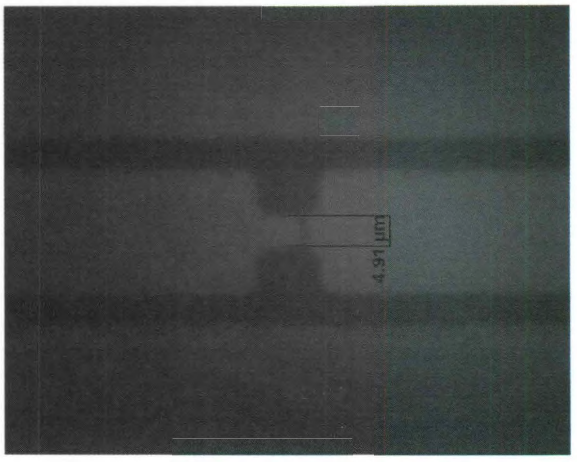

Figure 4.6 : Optical microscopy image of the dipole of one typical photoconductive antenna for THz emission or detection.

the photoconductive antenna Prof. Tonouchi provided us. During experiments, both the emitter and detector were mounted on non-magnetic XYZ stages. Also, a pair of hemisphere silicon lenses were attached to their bottoms each to further focus the spherical THz waves. Their metallic (golden) electrode pads were soldered with thin golden wires, the other ends of which were connected to SMA connectors and then BNC cables, and then a DC voltage supplier (for emitter) and a current preamplifier (for detector), separately.

Our second-version THz emitter is a commercial <110> ZnTe nonlinear crystal mounted on a rotatory stage.

4.2.4 Preamplifier and lock-in amplifier

The photocurrent signal proportional to the THz electric field was sent to a current preamplifier (shown in Fig. 4.7, top) through BNC cable, amplified, and then sent to a lock-in amplifier (SR830, Stanford Research Systems). The lock-in amplifier (shown

Figure 4.7 : Current preamplifier (top) and lock-in amplifier (bottom).

in Fig. 4.7, bottom) worked for a specific referenced-in chopping frequency from the mechanical chopper on the THz generation side to collect the (THz) signal at that frequency, and at the same time sent that signal to the computer.

4.2.5 Purging box and sample holder

Water in the air absorbs some components of the THz electromagnetic wave and then significantly affects the THz spectrum with several major absorption lines (the

most prominent one at 0.557 THz). In order to avoid this, a purging box made of acrylic plastic was constructed to cover the THz emitter, THz detector, four parabolic mirrors and the sample (as shown in Fig. 4.8). During the experiment, a slow dry nitrogen flow was induced inside the purging box through the green pipe, and a humidity meter was located inside the purging box to read the humidity to make sure THz data was being taken while its value was under 5 percent. The THz emitter (detector) inside the purging box was connected to the DC voltage supply (current preamplifier) outside the purging box via SMA-BNC connections through the walls of purging box (bottom inset). A 1D motorized stage (MFA-CC, Newport Corp.), which was controlled by the same motion controller (ESP 300, Newport Corp.) as that for the time-delay stage, was mounted in the middle between the second and third parabolic mirrors, and a homemade sample holder was mounted on its top through another two-dimensional manual stage to fulfill the flexible positioning of the solid film samples to be measured (top inset). Its nearby imbedded plastic glove to the wall of the purging box realized some additional adjustments for the samples, including the rotatory adjustments of the aligned SWNTs films, which will be discussed in Chapter 5. For electrically sensitive measurements, the sample holder was replaced by a plastic one to avoid grounding and shorting.

Both the motion controller and the lock-in amplifier are communicating with the computer through GPIB cables, and the entire most recent THz-TDS setup is shown in a photograph in Fig. 4.9

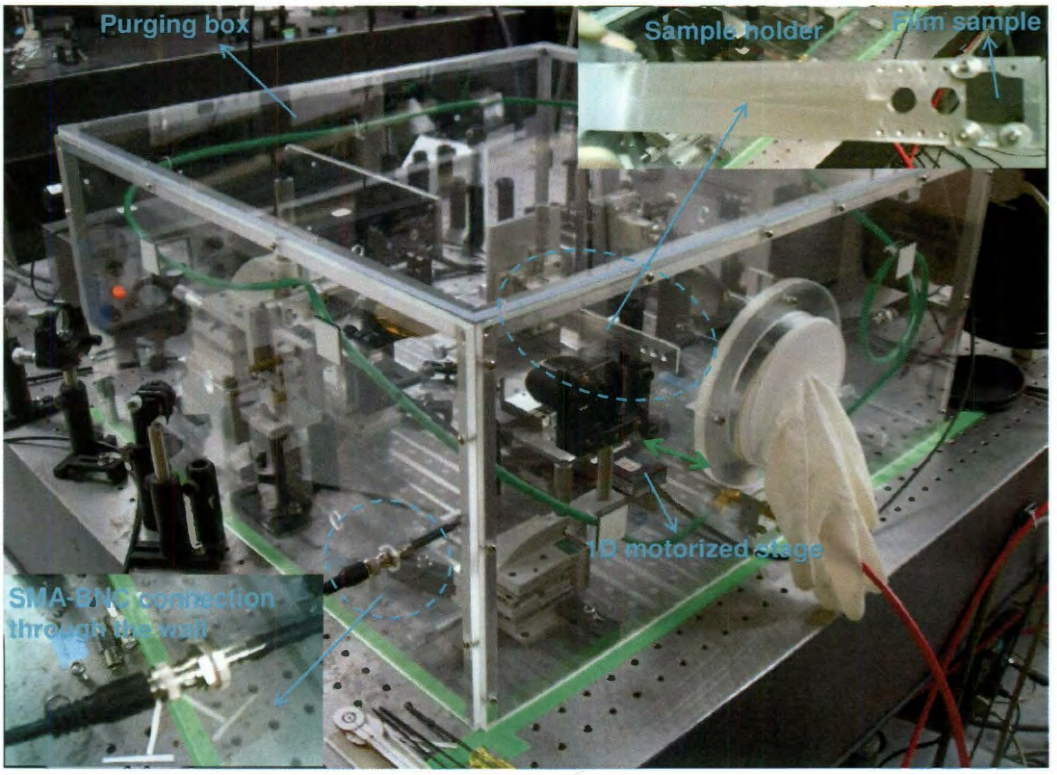

Figure 4.8 : Purging box for the THz-TDS system to avoid water absorption from air, with a homemade sample holder mounted on a 1D motorized stage inside it.

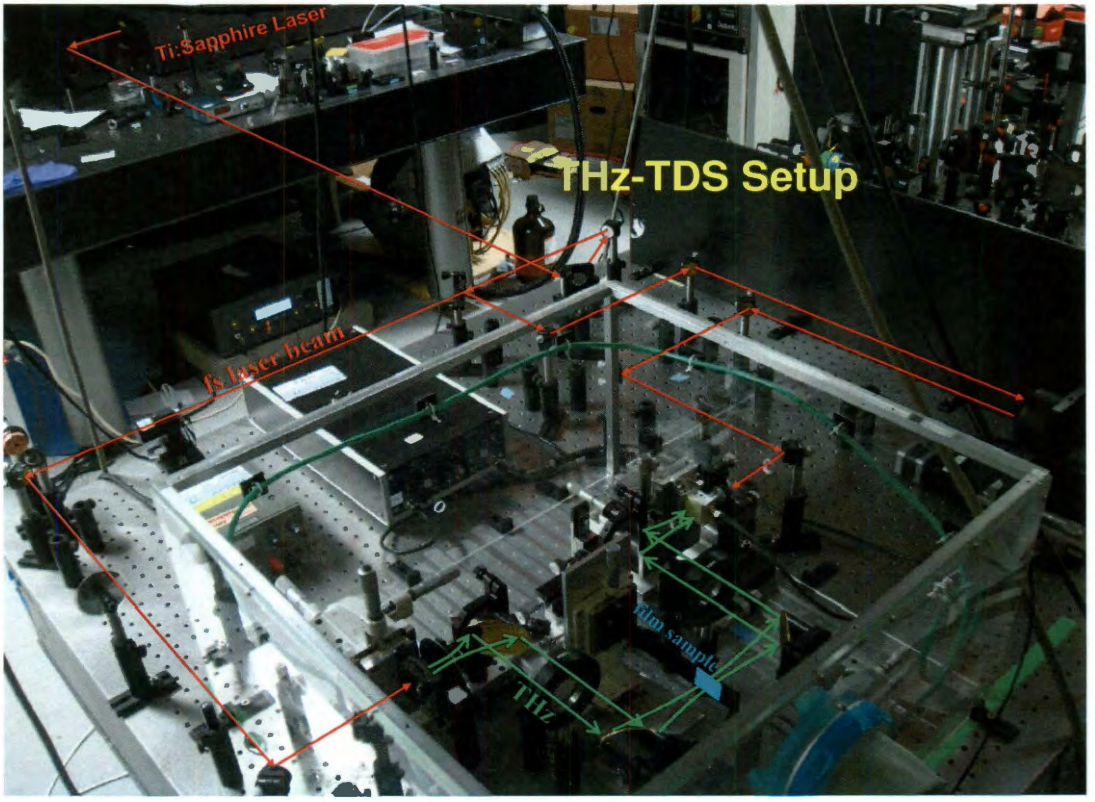

Figure 4.9 : Photograph of entire THz-TDS system.

Chapter 5

Experimental Results I : Carbon Nanotube THz Polarizer

5.1 Conventional industrialized wire-grid THz polarizer

Applications in THz technology are progressing at a rapid rate in concert with new compact techniques to produce THz radiation [101–105]. The potential applications of THz technology are diverse, as THz radiation provides a unique medium for non-invasive imaging, communications, and sensing devices that are currently being developed on both a research and industrial scale [101, 102]. Complementary to the development of this technology, it is not only important to devise ways to produce THz radiation, but also to have robust approaches to manipulate it and extract the detailed information contained within a coherent THz pulse. Currently, a host of wire-grid structures composed of uniformly spaced metal wires are employed as polarizers and filters for THz applications, which has already been widely commercialized and used. Such conventional THz polarizers are made by mechanically winding thin metallic strings, such as tungsten wires, on rigid frames under physical tensions. These THz polarizers are typically free-standing, and their function efficiencies rely highly on the wire spacing constants [106, 107]. Although these exhibit high extinction coefficients at THz wavelengths (> 25 dB), they have drawbacks of fragility and a structurally-tuned architecture that is not extendable to broadband THz operation.

5.2 Carbon nanotube THz polarizer

Here we describe results of polarization dependent THz transmission measurements on a strongly absorbing film of highly aligned SWNTs, which demonstrate extremely high anisotropy. Strikingly, when the THz polarization was perpendicular to the alignment axis, no absorption was observed within our experimental sensitivity despite the macroscopic thickness (~ 2 μm) of the film; when the polarization was parallel to the alignment direction, there was strong absorption. The degree of polarization in terms of absorbance was 1 and the reduced linear dichroism was 3, throughout the entire frequency range of our experiment ($0.2 - 1.8$ THz). These observations are a direct result of the one-dimensional (1D) nature of conduction electrons in the nanotubes and, at the same time, demonstrate that any misalignment of nanotubes in the film must have characteristic length scales much smaller than the wavelengths used in these experiments (1.5 mm to 150 μm). All these findings suggest that this type of aligned SWNT film performs as an ideal linear polarizer in the THz frequency range [96].

5.3 Experimental configuration

The growth and transfer of the highly aligned SWNT film is described in Chapter 4 in detail. The result of the contact transfer process is a homogeneous film (initially $\sim$ 2 μm thick) that remains as-grown, highly aligned, and free of exposure to any sort of solvent or liquid. Figure 5.1(a) shows a top-down scanning electron microscope image of the SWNT alignment present in such a transferred film, emphasizing the high degree of alignment, which makes this film well-suited for the study presented in this work.

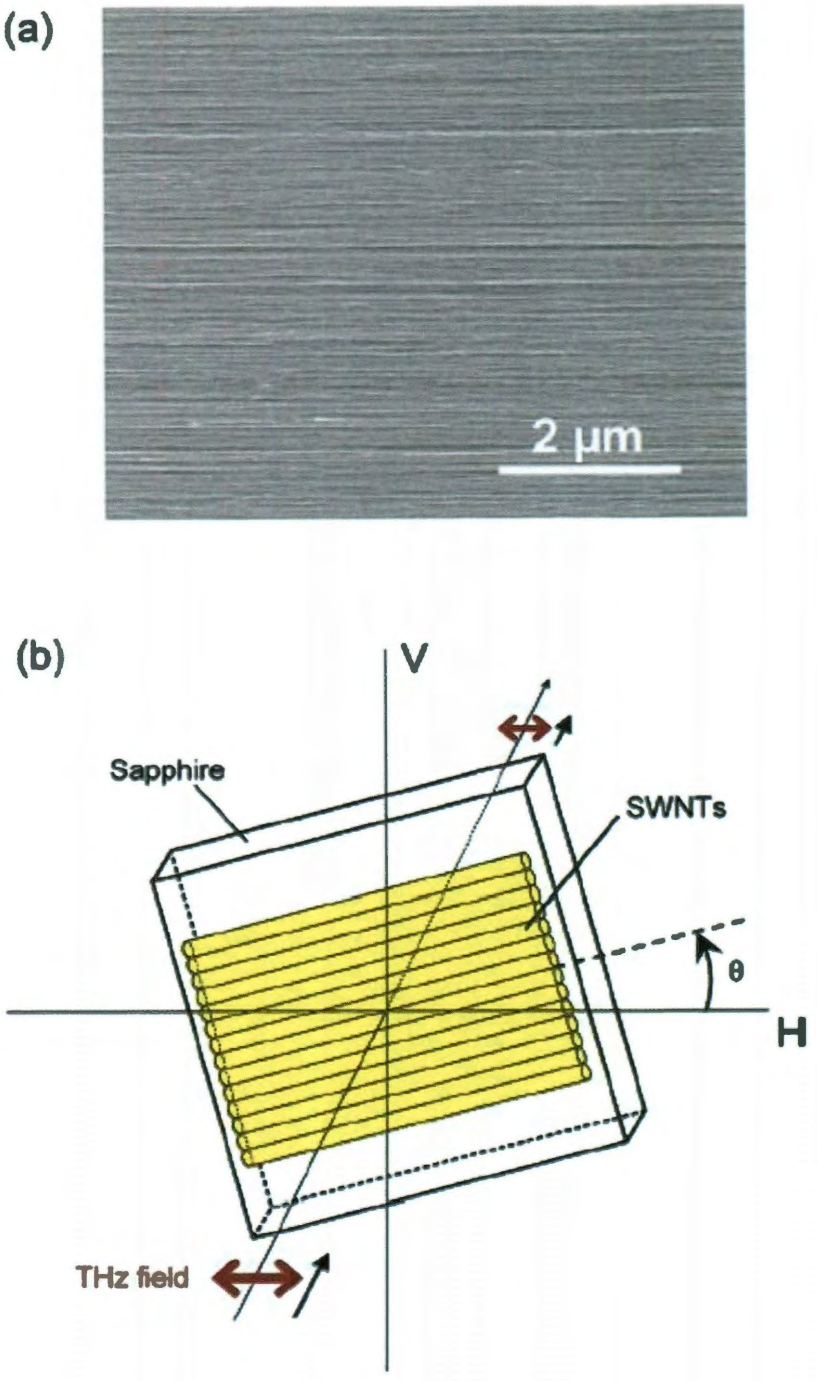

Figure 5.1 : (a) Scanning electron microscope image of the highly horizontally aligned SWNTs film used in this experiment. (b) Sketch of the experimental configuration used, showing the interaction between the linearly polarized THz electric field and highly aligned SWNTs film. The angle between the THz polarization direction and the nanotube alignment direction, θ, was varied between 0° and 90° [96].

The THz setup we utilized to study this SWNTs sample was described in Chapter 2 and Chapter 4. The THz beam obtained from the emitter was already highly linearly polarized, but a free-standing wire-grid polarizer with a degree of polarization of more than 99% in this range was placed in the path of the incident THz beam (8 in. both from the emitter and sample) to ensure the high degree of polarization of the THz beam incident on the sample. As schematically shown in Fig. 5.1(b), the SWNT sample was rotated about the propagation direction of the THz wave, which changed the angle, θ, between the nanotube axis and the THz electric field polarization direction from 0° to 90°. Thus, polarization-dependent THz transmission measurements were performed on both the SWNT film sample on a blank sapphire substrate and a reference sapphire sample with the same thickness as the sample substrate.

5.4 Results

5.4.1 Strong anisotropic THz responses

Figure 5.2(a) shows time-domain waveforms for THz waves transmitted through the reference sapphire (black dashed curve) and the SWNT film (solid colored curves). The different colors represent different angles θ between the THz polarization direction and the nanotube alignment direction. For the $\theta = 90°$ case, the signal was essentially the same as that of the reference, which means that there was virtually no interaction when the nanotube axis was perpendicular to the THz electric field. For the $\theta = 0°$ case, the signal was the smallest, which means that, when the nanotube axis was parallel with the THz electric field, the interaction was the strongest. From the $\theta = 45°$ and 30° cases, we see that the transmitted THz signal decreases monotonically

as θ decreases.

Figure 5.2(b) shows the amplitude spectra after Fourier transformation of the time domain data in Fig. 5.2(a) in a range of $0.2 - 1.8$ THz, where the anisotropy is more obvious. Figure 5.2(c) shows the absorbance, $A = -\log_{10}(T)$, where T is the transmittance defined as $T = |\tilde{E}_s/\tilde{E}_r|^2$ and $\tilde{E}_s$ and $\tilde{E}_r$ are the complex THz signals in the frequency domain obtained through Fourier transform of the time domain data for the sample and reference, respectively. From this figure, we can clearly see that, as the angle θ increases from 0° to 90°, the absorbance of the SWNTs decreases monotonically. When $\theta = 90°$, the absorbance is zero throughout this frequency range. On the other hand, when $\theta = 0°$, the absorbance is finite and high; it increases with increasing frequency, reaching a value over 1.0 at 1.8 THz. The 30° and 45° absorbance lines show the same trend as the 0° curve but with smaller amplitudes. The increasing absorbance with frequency in this spectral range is consistent with previous far-infrared spectroscopy results on various types of SWNT samples showing a robust absorption peak around 4 THz, whose origin is not understood [78, 79, 83, 86].

5.4.2 Extremely high alignment of the SWNTs

To quantify the degree of alignment of SWNTs in this film from these THz transmission data, we employ a data analysis procedure developed for studying anisotropic optical properties of SWNTs in the optical range [23–28]. Figure 5.3(a) plots the parallel ($A_{//}$) and perpendicular ($A_{\perp}$) absorbance spectra, corresponding to $\theta = 0°$ and 90°, respectively, together with $A_0 = (A_{//} + 2A_{\perp})/3$, which is the isotropic absorbance [108]. This physical quantity represents the absorbance expected if the nanotubes were randomly oriented. Finite alignment moves up (down) $A_{//}$ ($A_{\perp}$) with respect to A_0 and induces a finite linear dichroism, $LD = A_{//} - A_{\perp}$, shown in Fig.

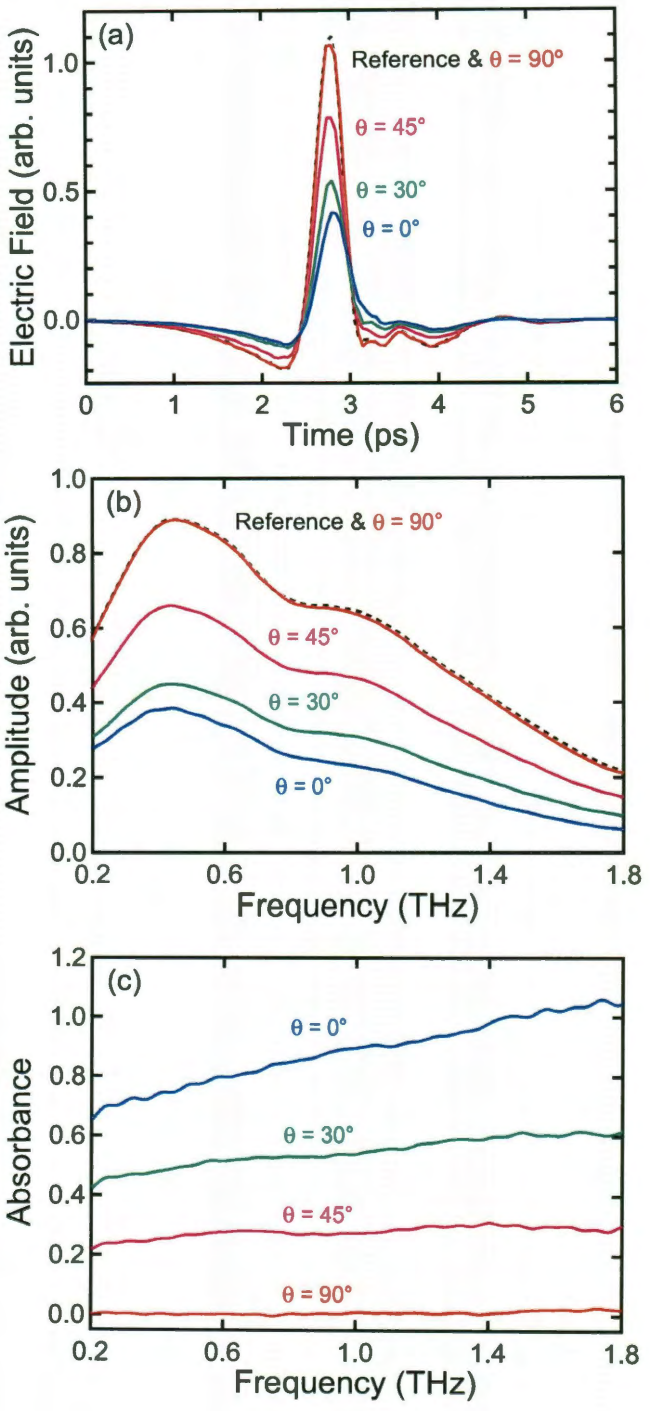

Figure 5.2 : (a) THz electric field signals in the time domain, (b) transmitted THz amplitude spectra obtained through Fourier transform of the time domain signals in (a), and (c) THz absorbance spectra for the reference sapphire substrate (black dashed curves) and for the SWNTs film for different polarization angles (colored solid curves) [96].